The magmatic and eruptive evolution of the 1883 caldera-forming eruption of Krakatau: integrating field- to crystal-scale observations

Madden-Nadeau, A.L.[1*], Cassidy, M.[1], Pyle, D.M.[1], Mather, T.A.[1], Watt, S.F.L.[2], Engwell, S.L.[3], Abdurrachman, M.[4], Nurshal, M.E.M.[4], Tappin, D.R.[5,6] & Ismail, T.[7]

amber.madden-nadeau@univ.ox.ac.uk

[1]Department of Earth Sciences, University of Oxford, South Parks Road, Oxford OX1 3AN UK

[2]School of Geography, Earth and Environmental Sciences, University of Birmingham, Edgbaston, Birmingham B15 2TT UK

[3]British Geological Survey, The Lyell Centre, Research Avenue South, Edinburgh, EH14 4AP UK

[4]Faculty of Earth Sciences and Technology, Institut Teknologi Bandung, Jalan Ganesa No. 10 Bandung 40132, West Java, Indonesia

[5]British Geological Survey, Nicker Hill, Keyworth, Nottingham NG12 5GG, UK

[6]Dept. of Earth Sciences, University College, London, WC1E 6BT, UK

[7]Department of Geology, Sekolah Tinggi Teknologi Mineral Indonesia, Bandung 40263, West Java, Indonesia

Abstract

Explosive, caldera-forming eruptions are exceptional and hazardous volcanic phenomena. The 1883 eruption of Krakatau is the largest such event for which there are detailed contemporary written accounts, allowing information on the eruptive progression to be integrated with the stratigraphy and geochemistry. Freshly-exposed sequences of the 1883 eruptive deposits of Krakatau, stripped of vegetation by the 2018 tsunamigenic flank collapse of Anak Krakatau, shed new light on the eruptive sequence. Whole-rock data, in context of the stratigraphy, shows that the pre-eruptive magmatic system was not a simple zoned magma reservoir, as previously hypothesised. Instead, a new model for the magmatic plumbing is proposed. Matrix glass analysed throughout the eruptive sequence indicates the presence of a shallow, silicic reservoir that was evacuated during the early eruptive activity from May 1883 onwards. Disruption of the shallow magma reservoir led to the coalescence and mixing of separate melt lenses, as evidenced by complex and varied plagioclase phenocryst zoning profiles. This mixing, over a period of two to three months, culminated in the onset of the climactic phase of the eruption on 26th August 1883. Pyroclastic density currents, emplaced during this phase of the eruption, show a change in transport direction from north east to south west, coinciding with the deposition of a lithic lag breccia unit. This may be attributed to partial collapse of an elevated portion of the island, resulting in the removal of a topographic barrier. Edifice destruction potentially further reduced the overburden on the underlying magmatic system, accelerating eruption rates, leading to the most explosive and energetic phase of the eruption in the morning of 27th August 1883. This phase of the eruption culminated in a final phase of caldera collapse, which is recorded in the stratigraphy as a second lithic lag breccia. The massive ignimbrite deposits emplaced during this final phase contain proximal lava blocks up to 8 m in size, observed for the first time in 2019. This study provides new evidence for the role that precursory eruptions and top-down driven amalgamation of shallow crustal magma bodies potentially play in the months leading up to caldera-forming eruptions.

Keywords: Caldera, stratigraphy, petrology, geochemistry, fieldwork

1. Introduction

The 1883 eruption of Krakatau (or Krakatoa) is one of the most infamous volcanic disasters, and the first caldera-forming eruption in history to make headline news around the world (Symons et al., 1888). The eruption demonstrated that violent, caldera-forming eruptions can have not only devastating local effects, but also global impacts (Verbeek, 1884; Symons et al., 1888; Simkin and Fiske, 1983). Subsequent work on other caldera-forming systems shows that these high-magnitude, low-frequency events may have very long build-up phases, characterised by both effusive and weakly explosive activity (e.g., Forni et al., 2018; Druitt et al., 2019). Long-term shifts in eruptive style are generally poorly understood, and in particular forcaldera systems. the The opportunity to monitor a volcano during the long build-up phase prior to a caldera-forming eruption has been lacking, making it harder to apply geophysical data in volcano monitoring (e.g., Druitt et al., 2012; Gottsmann and Marti, 2008; Newhall and Dzurizin, 1988). Petrological tools offer a unique insight into the architecture of the pre-eruptive magma plumbing system, and the conditions leading up to these explosive events. The 1883 eruption of Krakatau is particularly useful in this regard, as it is the largest eruption with observations documented in multiple contemporary written accounts, allowing the eruptive progression to be integrated with other datasets.

Physical and chemical properties of a magma will influence its ascent rate and ability to outgas, which are in turn strongly linked with eruptive style (Cassidy et al., 2018). Petrological data enable pre-eruptive magmatic conditions, such as pressure, temperature and volatile content, to be constrained. This in turn can provide constraints on the magma storage system. Pressure estimates can be used to infer magma storage depths, and temperature estimates are a key parameter when estimating timescales of magmatic processes (Kilgour et al., 2014). In addition, petrological data can provide information on magmatic processes like mafic recharge, magma mixing, assimilation and fractional crystallisation (e.g., Cassidy et al., 2015; 2016).

Past studies place some constraints on the structure of the upper-crustal magma storage system at Krakatau. Mandeville et al. (1996a) proposed that a chemically and thermally-zoned magma reservoir between 5 and 8 km depth, fed the 1883 eruption. Dahren et al. (2012) analysed the structure of the plumbing system beneath Anak Krakatau, the post-caldera volcano that emerged above sea-level in 1927. Using petrological methods and seismic tomography, they inferred that magmas stalled in three main lithologically-controlled zones: 23 – 28 km (plagioclase crystallisation), 7 – 12 km (clinopyroxene) and 3 - 7 km (plagioclase). The only constraints placed on water content of the melt come from loss on ignition (LOI) by difference of glass analyses at 4 +/- 0.5 wt% (Mandeville et al., 1996a). This study seeks to provide further constraints on critical magmatic storage conditions (temperature, pressure, H_2O content, fO_2) prior to the 1883 eruption.

There is still debate regarding the main triggers involved at various stages of the 1883 eruption. Potentially important processes include (i) fractional crystallisation, potentially leading to “second boiling” (Mandeville et al., 1996a; Camus et al., 1987), (ii) magma mixing (Francis and Self, 1983; Self and Wohletz, 1983) and (iii) phreatomagmatism, which has been proposed as a trigger for the main explosions on the morning of 27th August (Verbeek, 1884). Self and Rampino (1981) ruled out phreatomagmatism as they found no textural evidence for interaction of the deposits with water. Verbeek (1884) reported that two distinct ash compositions were erupted during May 1883: dacite and a high-alumina basalt (Stehn 1929). This led Francis and Self (1983) and Self and Wohletz (1983) to suggest that magma mixing triggered the initial stage of the Krakatau 1883 eruption. Several studies have also noted the presence of rare, banded pumice clasts from the main phase of the eruption (e.g., Self and Rampino 1981), which is often used as an indicator for magma mixing (Sparks et al., 1977). However, the two visually distinct glasses are of very similar chemical compositions (Self, 1992). Mandeville et al. (1996a) and Camus et al. (1987) suggested that crystal fractionation was the most important process prior to the 1883 eruption, increasing the SiO_2 content of the residual melt, whilst also enriching it in volatiles. Both factors make an eruption more likely and potentially more explosive (Blake, 1984). A final process that has been recognised for both Anak Krakatau and the 1883 system is assimilation of crustal material (Gardner et al., 2013). In order to evolve Anak's basaltic andesite products to 1883 compositions, whilst accounting for Sr isotopic compositions of plagioclase, Gardener et al. (2013) argue that 23 % assimilation of carbonate and/or quartzo-feldspathic siltstone would be required along with 45 % crystallisation of the basaltic andesite host magma.

The aim of this study is to integrate the known eruptive progression at Krakatau in 1883 – based on historical accounts – with new studies of the stratigraphy, crystal zoning and glass geochemistry. The new exposure of pyroclastic sequences from the 1883 eruption by the tsunami generated by the flank collapse of Anak Krakatau in December 2018 (Grilli et al., 2019), means that it is possible to build significantly on prior work (e.g., Mandeville et al., 1996a; and Self, 1992). Whole-rock and matrix glass data were collected and analysed in the context of this sequence and help to constrain the chemical structure of the plumbing system, allowing the magma reservoir zonation hypothesis to be tested. Thermodynamic modelling using Rhyolite-MELTS provides further insight into the role of fractional crystallisation prior to the 1883 eruptions. Chemical analyses of both plagioclase and pyroxene phenocrysts at a much higher spatial resolution than has been previously published (e.g., Mandeville et al., 1996), allow the crystal growth history to be constrained in more detail. Furthermore, thermobarometic and hygrometric models provide improved constraints on magmatic conditions. These field observations, together with geochemical and petrological data, shed new light on this highly-active caldera system and provide a new context for the monitoring of the present-day activity of Anak Krakatau.

2. Geological Context

2.1 Tectonic setting

The Krakatau complex four islands: Panjang, Sertung, Rakata, and Anak Krakatau (figure 1). Panjang and Sertung are remnant islands left behind after a caldera-forming eruption prior to that in 1883; Rakata is the southern remnant of a pre-existing larger island that lay between Panjang and Sertung, the northern two thirds of which was destroyed in 1883 (dashed line, Figure 1). Prior to the 1883 caldera collapse, this main island of Krakatau consisted of three volcanic centres aligned NNW: Perboewatan, in the north, Danan, in the centre, with Rakata forming a higher peak to the south (Figure 1). Anak Krakatau is the current subaerial volcanic cone, which first emerged above sea-level in 1927, on the same alignment as the 1883 vents, and is located approximately between the positions of Perboewatan and Danan.

The Krakatau archipelago is part of the Sunda Arc; volcanism in this region is caused by subduction of the Indo-Australian Plate beneath the Eurasian Plate (Figure 1). Krakatau is located in the Sunda Strait, between Java and Sumatra, at the intersection of a NNE trending lineament of quaternary volcanic edifices roughly perpendicular to the Java trench (Nishimura et al., 1992) and a fault connecting Krakatau with the Sunda Graben (e.g. Harjono et al., 1989). The entirety of the Sunda Strait is experiencing active extensional tectonics as Sumatra is rotating relative to Java; this rotation has been 20° since the late Cenozoic (Hall, 2012; Hall and Spakman, 2002; Ninkovich, 1976). Therefore, magmatism in the Sunda Strait is not only a function of subduction, but also of rifting and extension (Harjono et al., 1989), associated with the thinning of the subducting slab and mantle upwelling beneath Krakatau (Abdurrachman et al., 2018).

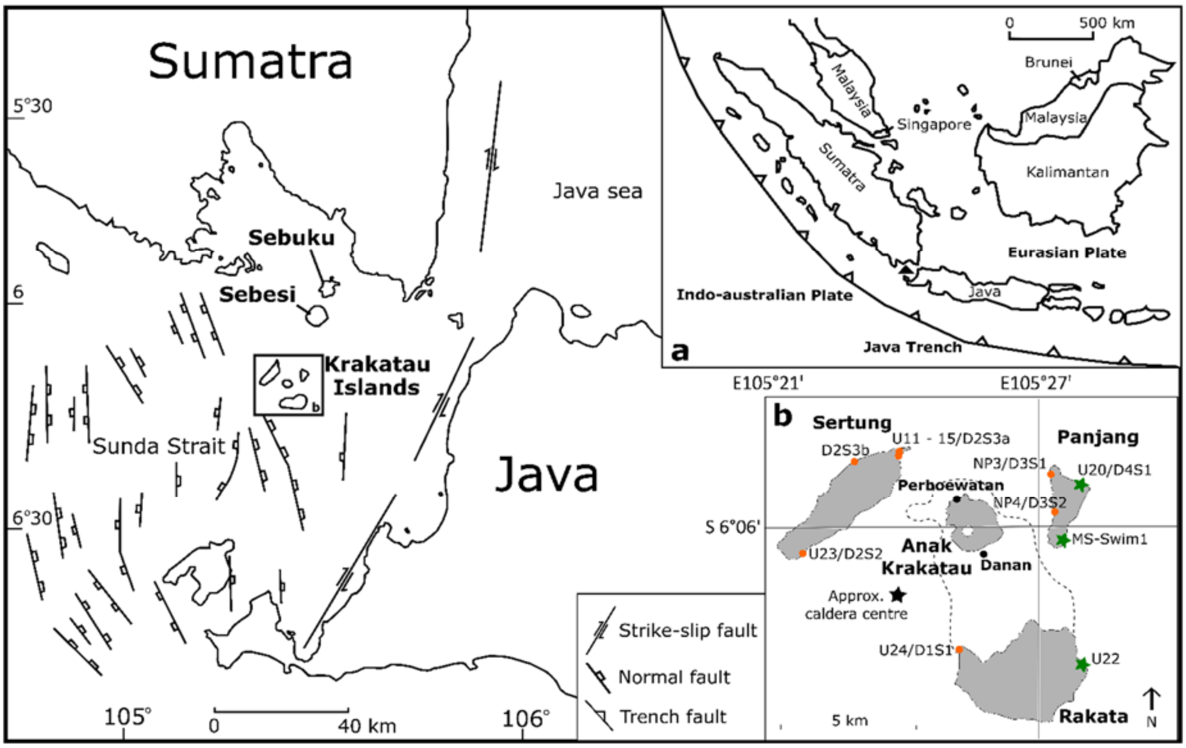

Figure 1: Tectonic map showing the Sunda Straits, with insert (a) showing the Java trench and (b) showing the Krakatau islands and field sites visited. The green stars in insert (b) are new field sites, presented here for the first time, whereas localities matching, or very close to, the orange circles were also visited by Mandeville et al. (1996) and Self and Rampino (1986). Localities with two names were visited in both field campaigns (2017 and 2019). All sites visited had considerably more exposure than observed and/or presented prior to 2019, due to erosion by the 2018 tsunami associated with a flank collapse on Anak Krakatau. The black star labelled approximate caldera centre marks the deepest part of the caldera structure, estimated from bathymetric data from Deplus et al. (1995). The dotted line represents the island prior to collapse in 1883, with Perboewatan and Danan, the 1883 active cones marked as black circles. Figure based on Mandeville et al. (1996a), Schlüter et al. (2002), Lunt et al. (2009), Susilohadi et al. (2009) and Dahren et al. (2012).

2.2 Pre-1883 eruptive history

The ages of pre-1883 eruptions are uncertain. Drill core data suggests an eruption in the Sunda Straits at ca. 60 ka, however this cannot be definitively attributed to Krakatau (Ninkovich, 1979). The Javanese chronicle the Book of Kings, Pararaton (1869), describes a very large eruption, with “heavy rains of stone” in 416 AD originating from the straits of Sunda (Symons et al., 1888). However, there has not been any geological evidence presented to date to substantiate this eruption. In May 1681, observations of earthquakes and pumice were made in the diaries of Johann Wilhelm Vogel and Elias Hesse, most likely pertaining to an eruption of Krakatau (Verbeek, 1884; Vogel, 1690; Hesse, 1690; Hesse, 1694).

2.3 1883 Eruption

The eruption of Krakatau volcano in August 1883 was the culmination of at least four months of unrest (Figure 2). The climactic eruption ejected 18 – 21 km^3 (9 – 10 km^3 dense rock equivalent; Self and Rampino, 1981) of ejecta in a sequence of pyroclastic density currents (PDC) that swept across the straits of Sunda and caused volcanogenic tsunamis, that in total killed approximately 36,000 people (Self, 1992). This eruption resulted in the destruction of two-thirds of the main island of Krakatau, forming a submarine caldera, which manifests today as a 250 m depression in the seafloor (Deplus et al., 1995). The soundwaves produced from the eruption were the greatest ever recorded in the audible range (Gorshkov, 1959), and the atmospheric effects were seen around the world, with vivid sunsets observed up to a year after the eruption (Symons et al., 1888; Self, 1992).

The first record of the 1883 eruption of Krakatau is for 20th May, with contemporary descriptions suggesting Vulcanian to Sub-Plinian activity from the edifice Perboewatan (Verbeek, 1885). The activity reduced after 22nd May (Symons et al., 1888). Self (1992) suggested that the eruption column at this stage reached 20 km, with extensive ash fall (~375 km away). There are no records of activity between 23rd and 26th May (Symons et al., 1888); on 27th May a party visited the island and observed explosions every 10 minutes (Verbeek, 1885). There are no specific records from 28th May to 19th June, however, Krakatau was reported to have continuously expelled 'smoke' throughout June, according to the newspaper *Javasche Courant*, and Symons et al. (1888) report no interruption in activity "according to reports from lighthouses… and vessels". The height of the plume likely increased on 19th June as it was observed from the coast of Java (Simkin and Fiske, 1983) (Figure 2).

On 24th June, a second column of 'smoke' was observed from Java for the first time, likely emanating from the edifice Danan. This was coincident with the reported disappearance of the summit of Perboewatan (Symons et al., 1888). However, this is not mentioned by Ferzenaar, who was the last person to set foot on the island (11th August) prior to the climactic phase of the eruption; he instead reported that Danan had partially collapsed (Verbeek, 1885). There are few records throughout July, however Symons et al. (1888) state that there were "continued eruptions, earthquakes and occasional violent explosions". Verbeek (1885) observed "no ash" on 3rd July and instead reported "a hazy red glimmer", which suggests activity had decreased in this period.

The onset of Plinian activity began on 26th August (Figure 2). At 2pm local-time, a black eruption column rose ~ 26 km into the atmosphere, with explosions every 10 minutes (Sturdy, 1884). By 3pm, the explosions were heard ~ 670 km away (Symons et al., 1888), and the first abnormal sea wave was recorded (Latter, 1981). By 5pm the explosions were being heard all over Java (Symons et al., 1888). There was intense volcanic lightning all through the night and a strong sulphurous smell was reported on nearby ships, such as the Charles Bal (Sturdy, 1884).

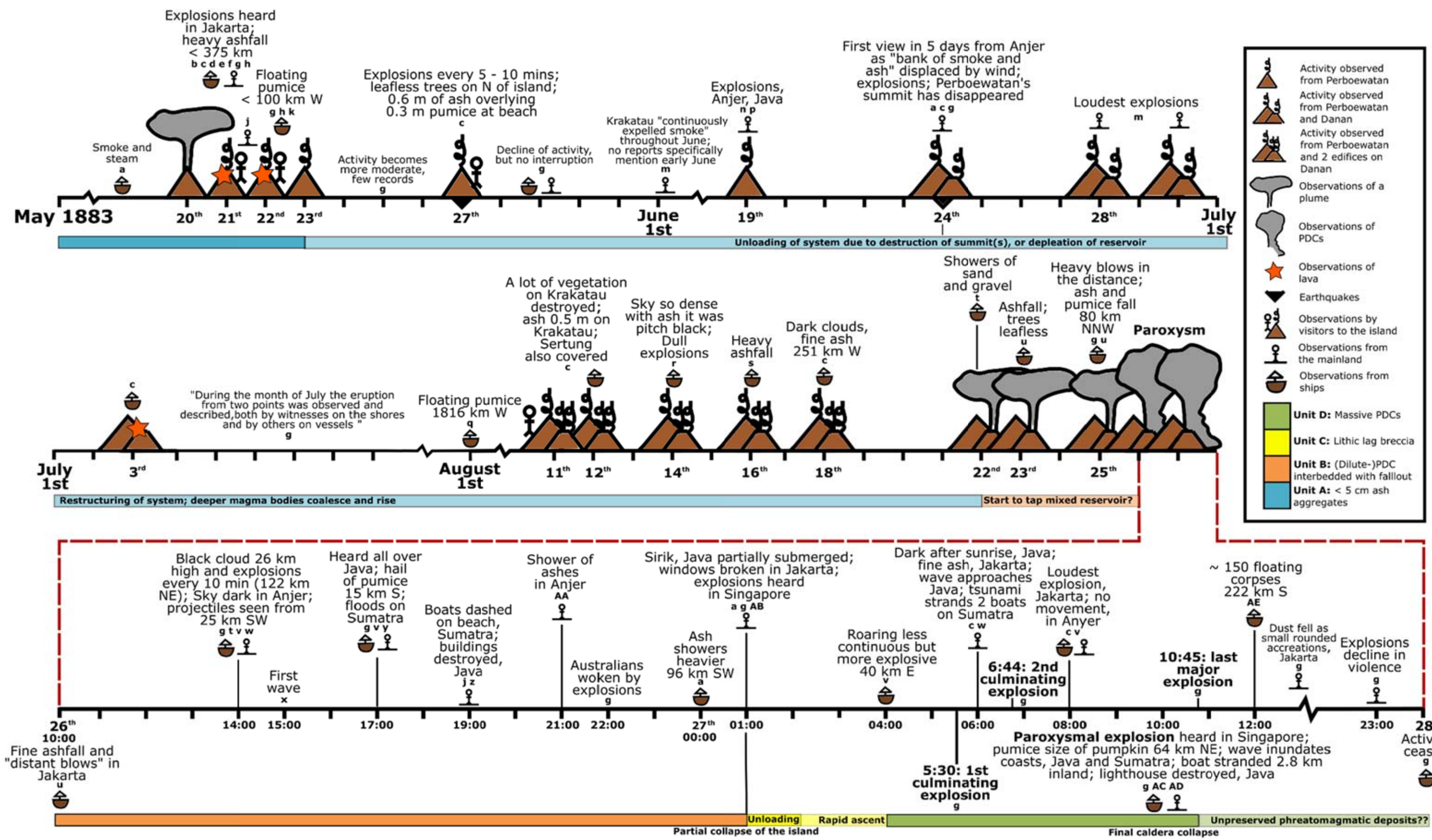

Figure 2: Schematic diagram showing the timeline of the eruption as given by various eye witness accounts. The accounts from which the information is taken is represented by letters, as follows: (a) Tenison-Woods (1884), (b) Times of London 03/06/1883, (c) Verbeek (1885), (d) Captain Walker 16/06/1883, (e) MacKenzie, Java Bode 30/05/1883, (f) Tagliche Rundchau (1883), (g) Symons et al. (1888), (h) Grainger, Algmeen Dagblad 23/05/1883, (j) Furneaux (1964), (k) Sulzer, Java Bode 30/05/1883, (m) Javasche Courant, 20/07/1883, (n) Algemeen Dagblad, 20/06/1883, (p) Algemeen Dagblad, 26/06/1883, (q) Ashdown (1883), (r) Bataviaasch Handelsblad, 16/08/1883, (s) Algemeen Dagblad, 17/08/1883, (t) Joly (1885), (u) van Heerdt, report in RS archives, (v) Sturdy (1884), (w) Metzger (1884), (x) Latter (1981), (y) Algemeen Dagblad, 11/09/1883, (z) Algemeen Dagblad, 05/09/1883, (AA) Bataviaasch Handelsblad, 09/09/1883, (AB) Algemeen Dagblad, 27/08/1883, (AC) Ceylon Observer 06/09/1883, (AD) Algemeen Dagblad, 03/09/1883, (AE) Times of London, 08/10/1883.

Interpretations regarding the eruptive progression have been made from this, and then has been combined with information of the 4 units in the 1883 eruptive deposits. All page numbers for historical references can be found in supplementary material 1.

The most powerful explosions, based on pressure deviations recorded on the Batavia gasometer record (Latter, 1981), occurred at 5.30 am, 6.44 am, ~10:00 am and 10.45 am on 27^{th} August (Symons et al., 1888); the third of these was the most violent, and was heard in Singapore (Strachey 1888). Multiple tsunami waves traversed the Sunda Straits from the 26^{th} to 27^{th} August, and were the cause of the vast majority of casualties (Symons et al., 1888). By far the largest of these waves had an origin time of approximately 10 am on 27^{th} August (Verbeek, 1885; Latter, 1981), thus broadly coinciding with the most powerful recorded explosion. The whole of the northern portion of the island disappeared into the sea during caldera formation (Lindemann, 1884). However, the precise time of caldera collapse has not yet been determined (Self, 1992). Supplementary Material 1 gives page numbers for all historical references used.

2.4 Anak Krakatau

In 1927 Anak Krakatau or “child of Krakatau” emerged from the sea, forming a new subaerial volcanic cone (Stehn, 1929) that eventually became a permanent island, and has since grown rapidly. Since the 1960s when the active vent stopped interacting with seawater, Anak Krakatau has predominantly erupted effusively, punctuated with Vulcanian and Strombolian explosions (Abdurrachman et al., 2018).

A period of elevated activity from July to October 2018 culminated in the south western portion of Anak Krakatau collapsing on December 22^{nd} 2018. This created a volcanogenic tsunami which greatly impacted the coast along the straits of Sunda, killing 437 people (Grilli et al., 2019).

3. Methods and material

3.1 1883 Stratigraphy and samples

Field campaigns to the Krakatau islands were undertaken in September 2017 and August 2019. Some field locations, originally described by Mandeville et al. (1996b) and Self (1992), were revisited (Figure 1b). The 2019 field campaign provided new constraints on the stratigraphic sequence, as erosion associated with the December 2018 tsunami increased exposure of the 1883 sequence considerably at all localities. Stratigraphic logs were created from field observations, and cross correlated using lithological and stratigraphic characteristics, as well as volcanic glass chemistry.

In addition to samples collected on both field campaigns, samples (08 and 72) originally collected from the Norham Castle , (a ship that was 92 km from Krakatau in the Sunda Straits on 26th and 27th August 1883), and archived at the British Geological Survey (BGS), as well as a sample of ash (07) taken from "Districts of java opposite Krakatau and on volcanic island itself", were also analysed. All field locations and details on samples, are given in Analytical Data 1 which can be found in the dataset Madden-Nadeau (2020).

3.2 Vesicularity and crystallinity

To make first order estimates of vesicularity and crystallinity of the 1883 samples through the stratigraphy, thin sections of pumice clasts were made in the Department of Earth Sciences, University of Oxford. A transmitted light microscope was used to take five images of each sample. These were processed using image processing software to provide an average estimate of vesicularity, and crystallinity, reported on a vesicle-free (VF) basis. Estimates for vesicularity are likely to be slightly underestimated, as a result of the lower limit of vesicle size resolution, as well bubbles trapped within the resin during the sample preparation process and plane of section effects. Error will also be incurred as a result of the degree of thresholding chosen for each image. The reproducibility, determined using the same method 10 times on a single image, averaged over 5 images, incurs a 1 σ error in crystallinity estimates of +/- 0.1 % (0.7 % VF), and in vesicularity of +/- 2.5 %.

3.3 X-ray fluorescence (XRF)

A selection of samples collected through the 1883 stratigraphy were analysed for whole-rock major and minor element chemistry by X-Ray Fluorescence (XRF) at the Department of Geology, University of Leicester on a PANalytical Axios Advanced XRF spectrometer. The majority of these samples were powdered picked pumices, with the exception of one ash sample from a PDC deposit, U22.2 which was a very fine ash aggregate layer, as well as 4 samples which were bulk tephra. For the picked pumices, multiple clasts were powdered.

Major elements were determined on fused glass beads prepared from ignited powders, and include SiO_2, TiO_2, Al_2O_3, Fe_2O_3, MnO, MgO, CaO, NaO_2, K_2O, P_2O_5 and SO_2. Minor elements include As, Ba, Ce, Co, Cr, Cs, Cu, Ga, La, Mo, Nb, Nd, Ni, Pb, Rb, Sb, Sc, Se, Sn, Sr, Th, U, V, W, Y, Zn, Zr as well as Loss on Ignition (LOI).

3.4 Scanning electron microscope (SEM)

Back-scatter electron (BSE) images of plagioclase and pyroxene phenocrysts, picked from crushed pumice samples and mounted in resin blocks, were obtained with an FEI Quanta 650 field emission gun (FEG) SEM in the Department of Earth Sciences, University of Oxford, and a Zeiss Merlin Compact FEG-SEM at the Sir William Dunn School of Pathology, University of Oxford. Operating conditions were 20 KeV with a 15 micron aperture.

4.4 Electron Probe Microanalysis (EPMA)

Phenocryst phases were analysed on a FEG CAMECA SX-5 electron microprobe at the Department of Earth Sciences, University of Oxford. Sodium was always analysed first, at a 10 s peak count time, and secondary standards of a similar composition to the target were analysed to check the accuracy of the calibration.

Plagioclase phenocrysts were picked from archived ash collected at the time of the eruption, as well as samples collected in the field. Of the samples collected in the field, the majority of phenocryst samples were picked from multiple crushed pumices, with one ash sample, as well as two bulk tephra samples. Mineral traverses (n = 56) for Al, Si, Na, Ca, K, Fe, Ti, Mn and Mg were collected by EPMA for selected plagioclase phenocrysts at 15 kV acceleration voltage and 20 nA beam current, with 5 micron defocussed beam size. Fe, Mg and Ti were acquired again, along with Sr, under a 40 nA beam with longer peak count times of 270 s, following parallel transects (n = 16). Point spacings in line analyses were approximately 10 microns. Points were also analysed for BSE image calibration for anorthite content with the same operating conditions.

Quantitative traverse mineral analyses for pyroxene phenocrysts picked from archived ash collected at the time of the eruption (n = 46) were obtained at 15 kV, with a focused beam of 20 nA for Al, Si, Na, Ca, Fe, Ti, Mn, Cr and Mg. Fe/Ti oxides (n = 419) partially included into the rim of pyroxene phenocrysts from both archive and field samples, were also analysed as points under the same conditions.

Point analyses of matrix glass, mounted in resin, were analysed on a Jeol JXA-8200 electron Microprobe in the School of Archaeology, University of Oxford. Glass analyses were conducted at 15 kV with a 5 micron defocussed beam of 6 nA for Al, Si, Na, Ca, K, Fe, Ti, Mn, Mg, P and Cl. The majority of matrix glass was picked from crushed picked pumices samples, with 3 samples being predominantly ash, and one bulk tephra sample.

4.5 BSE image calibration for Plagioclase

Back-scatter electron intensity profiles of plagioclase phenocrysts were calibrated for anorthite content using quantitative point analyses, obtained via EPMA, in imageJ, following the approach outlined by Ginibre et al. (2002)., Where enough EMPA data was available some phenocrysts were calibrated individually, whilst a global calibration was used for other crystals where brightness and contrast settings on the BSE images made the images comparable.

4 Results

4.1 Fieldwork and stratigraphy

The stratigraphic sequence of the 1883 eruptive deposits has previously been established by Self and Rampino (1981) and Mandeville et al. (1996b), however, a collapse of the south-eastern flank of Anak Krakatau associated with the 2018 tsunami made this worth revisiting.. The stratigraphy as presented by Self (1992) (after Self and Rampino; 1981) and Mandeville et al. (1996b), are shown in figure 3. Self and Rampino (1981) produced a general proximal stratigraphy comprising sub-Plinian fall deposits interbedded with surge deposits up to 20 m thick, overlain by up to 55 m of massive ignimbrite deposit. Mandeville et al. (1996) reported a layer up to 4 cm of olive- to bluish-grey fine ash fall deposit, which they attributed to phreatomagmatic activity in the May to August period. This was located at the base of the 1883 deposits, overlying a soil horizon on West Rakata and West Panjang (equivalent to our localities U24/D1S1 and NP3/D3S1, respectively), followed by 5 - 20 cm of coarse light-grey pumice fallout. Overlying this is 4 to 6 m of fallout interbedded with surge deposits, followed by thick accumulations of massive PDC deposits. The thickness of the fallout layer is therefore disputed, with Self and Rampino (1981) observing fall deposits interbedded with surges up to 20 m thick, and Mandeville et al. (1996) observing up to 6.2 m of pumice fallout interbedded with surges. A log with stratigraphic correlations and field photographs for each locality are shown in Supplementary Material 2 – 9.

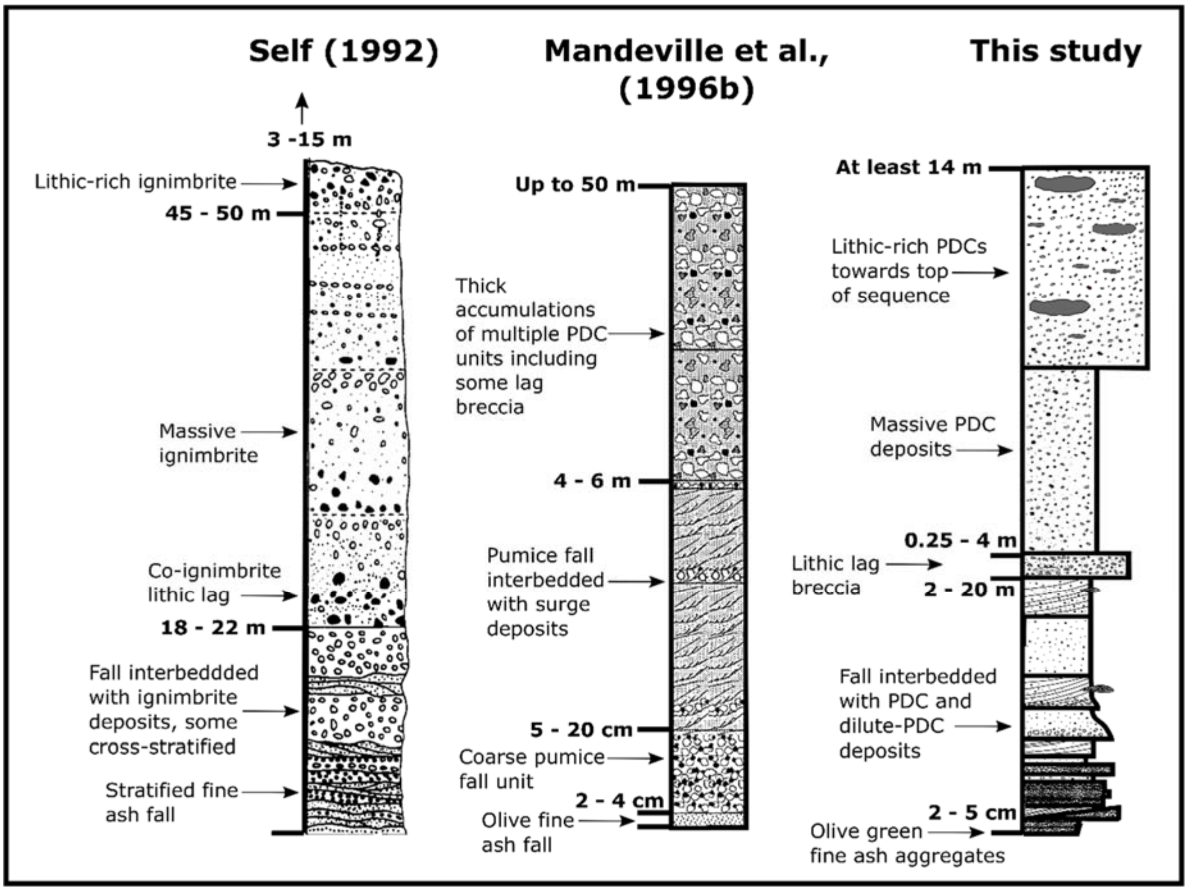

Figure 3: Composite logs of stratigraphy derived by Self (1992), Mandeville et al., (1996b) and this study, for comparison.

Our observations agree with Mandeville et al. (1996) in terms of the presence of a distinctive ash fall deposit at the base of the sequence (Figure 3), which we henceforth term “Unit A” (figure 4a). Unit A is between 2 and 5 cm thick and was only found exposed on West Rakata and South Panjang. This layer overlies a red paleosol, has a distinctive olive-green colour, and is composed of fine-ash aggregates.

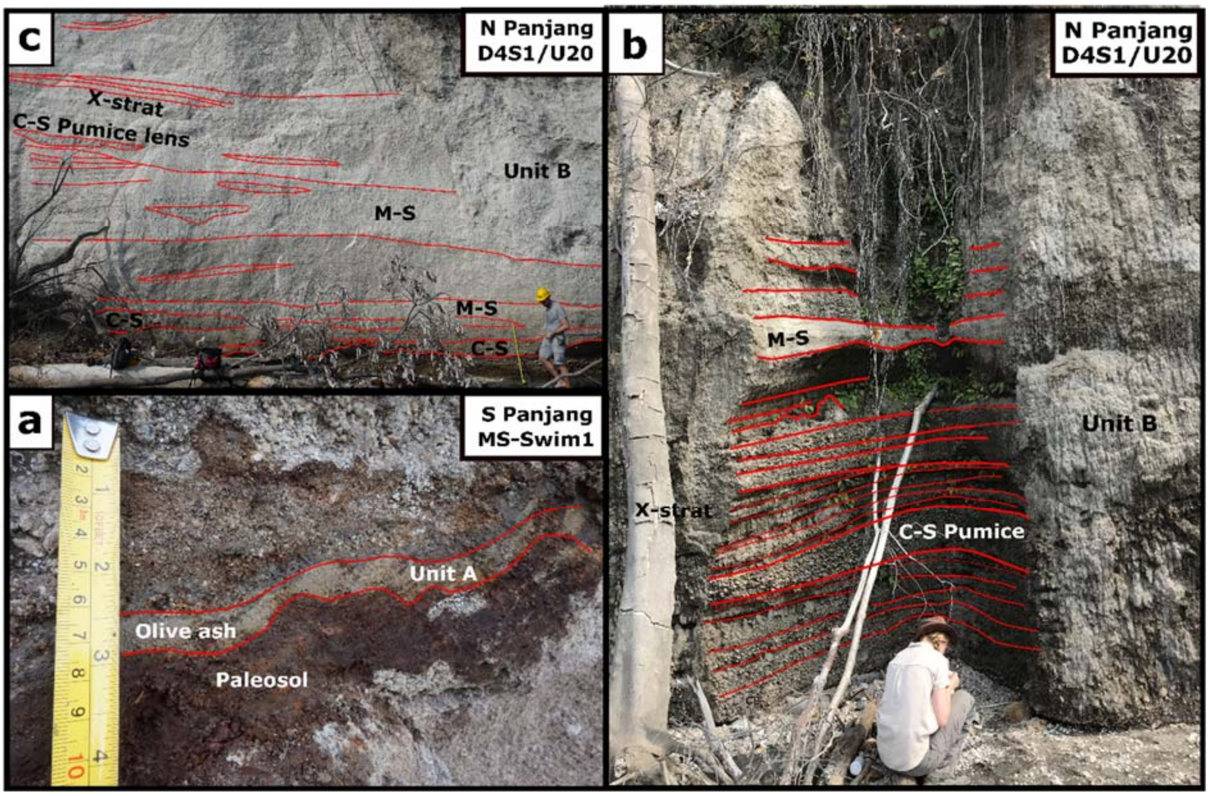

Figure 4: Panel (a) shows Unit A, as observed from locality MS-Swim1 on South Panjang, which is a thin layer of olive-green ash aggregates, overlying a red paleosol. Panel (b) shows the base of Unit B at locality D4S1/U20 on North Panjang, and is composed of clast-supported (C-S) fallout layers, interbedded with dilute PDCs that show cross-stratification (X-strat). Panel (c) shows the units overlying those in panel (b), at locality D4S1/U20. These are also part of Unit B, and show matrix-supported (M-S) dilute-PDCs interbedded with pumice-supported lenses. All locations are shown in Figure 1.

Unit B is characterised by well-sorted beds of angular lapilli, interbedded with poorly-sorted layers which are matrix-supported (Figure 4b; 4c; 5a). Clasts within the well-sorted layers are predominantly juvenile pumice (>80%), the remainder being dense, angular, and visibly-altered volcanic lithics; Mandeville et al. (1996b) determined that the majority of these lithics are basalt and basaltic andesite. Of the juvenile clasts, ~90% are white pumice, although pink, grey and yellow pumice are also observed. Clasts within the poorly-sorted units show similar proportions. Some of the poorly-sorted beds contain cross-bedding, thus these have been interpreted as dilute-PDC deposits (Branney and Kokelaar 2002). These dilute-PDC deposits also contain laterally-restricted, discontinuous lenses of well-sorted, sub-rounded, pumiceous lapilli. Unit B is thus interpreted to comprise fall deposits interbedded with PDC and dilute PDC deposits (Branney and Kokelaar 2002). Unit B is up to 20 m thick, agreeing with observations made by Self and Rampino (1981) (Figure 3) of a unit up to 20 m thick comprising fall deposits interbedded with surges. Charcoal and tree moulds were found towards the base of Unit B at two localities; carbonised logs were also reported by Mandeville et al. (1996), but were not attributed to a specific unit within the stratigraphy.

Next in the sequence is Unit C, which is characterised by lithic blocks (up to 50 cm) in a poorly-sorted, juvenile matrix (figure 5a; 5b). This section of the sequence is therefore interpreted to be a lithic lag breccia (Branney and Kokelaar, 2002; Druitt and Sparks, 1982). Both Self and Rampino (1981) and Mandeville et al. (1996b) identify lithic lag breccias in the sequence (Figure 3), however only Self and Rampino (1981) allude to them occupying the same stratigraphic horizon. The lag breccia is variable in stratigraphic thickness (0.3 to 4 m), and bifurcates in some outcrops (Figure 4a). The proportion of lithic blocks within this unit also varies between localities.

Unit D is a massive, poorly-sorted, matrix-supported unit containing predominantly pumice clasts (80-90% of clasts) in an ash-rich matrix (Figure 5b). Both Self and Rampino (1981) and Mandeville et al. (1996) identify a similar unit towards the top of the sequence (Figure 3). The structureless nature of Unit D suggests it was likely deposited by large volume, high-concentration PDCs (Branney and Kokelaar, 2002). Another characteristic feature of Unit D is the presence of obsidian clasts. Frothy, glassy, and banded obsidian clasts were observed (e.g., Shields et al., 2016), making it likely that at least some of the obsidian is juvenile (Self and Rampino, 1981). Black and white banded pumices were observed in low abundance, and were also identified by Self and Rampino (1981).

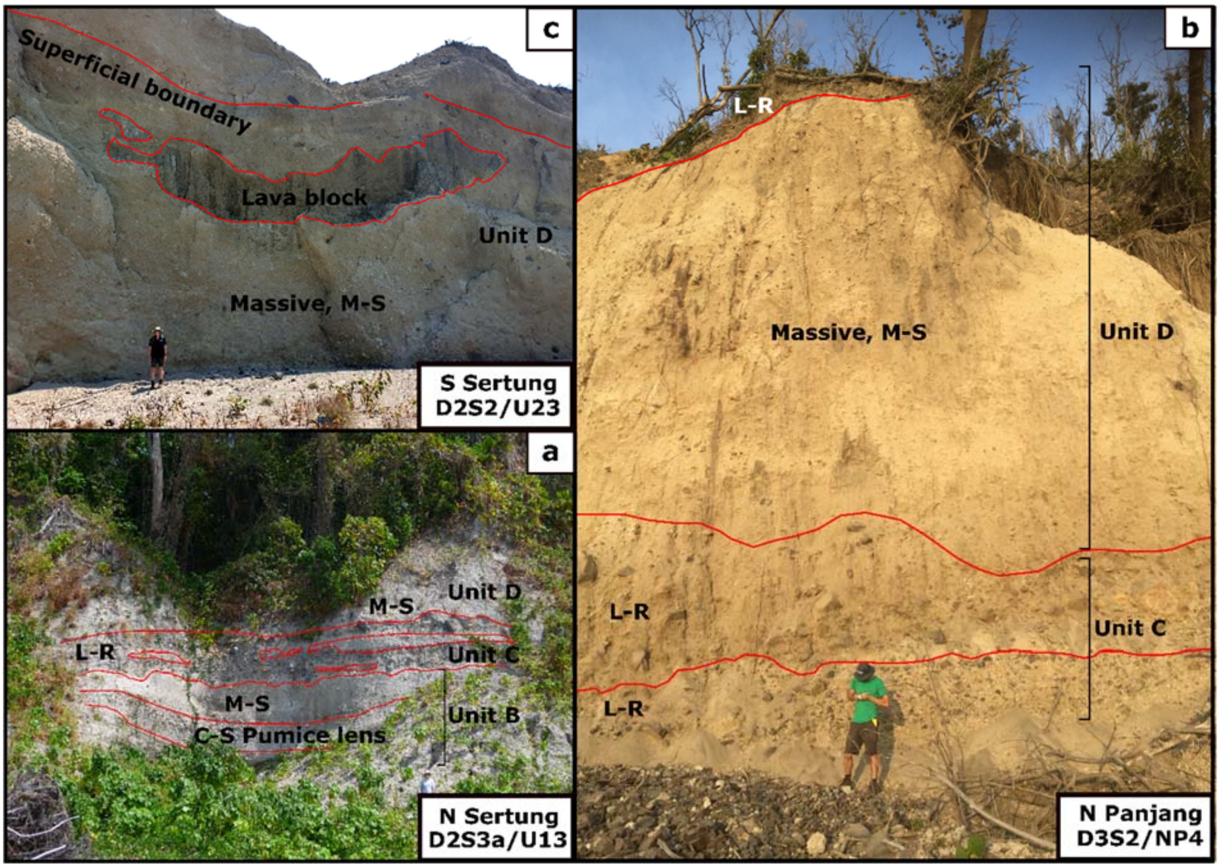

Figure 5: Panel (a) shows Units B, C and part of Unit D, as observed from locality D2S3a/U13, North Sertung. Unit B comprises clast-supported (C-S) pumice layers interbedded with matrix-supported (M-S) layers. Panel (b) shows Units C and D at locality D3S2/NP4, North Panjang. Unit C in both panels (a) and (b) show lithic-rich (L-R) layers. Panel (c) shows the top of Unit D at locality D2S2/U23, South Sertung. Unit D is comprised of massive PDC deposits in both panels (b) and (c). In panel (b), there is a second lithic-rich layer at the very top of the sequence. In panel (c) there are large lava blocks up to 8 m in size. All locations are shown in Figure 1.

A second lithic lag breccia is observed at the top of Unit D on North Panjang (Figure 4b), which concurs with an updated stratigraphic log presented by Self (1992) (Figure 3). In addition, new exposure on South Sertung (D2S2/U23, Figure 1) was observed for the first time in the August 2019 field campaign, and comprises large blocks of lava up to 8 m in length within a massive PDC unit (Figure 5c). Although the blocks are intact, they are intensely fractured and have sub-rounded irregular shapes, aligned broadly horizontally, but not confined to a single horizon within the massive PDC deposit (Figure 4c). Some of these fractured blocks look very similar to glassy obsidian clasts, with the same dark colour and a similar phenocryst content, whereas other blocks are grey in colour and duller. This section of Unit D also contains clasts of mudstone. We also noted crude horizontal stratification of the PDCs delineated by subtle colour changes; this was also observed in massive PDC units described by Mandeville et al. (1996).

Locality U22 (Figure 5) is the only outcrop where the entire sequence (Units A to D) can be observed. The sequence appears to be condensed (2.8 m), and we use this as a type locality. Key marker beds in the 1883 stratigraphic sequence include the thin, green, ash-aggregate layer overlying a red paleosol at the very base of the sequence (Mandeville et al., 1996b; Figure 3), delineating Unit A (figure 6a). Pumice fallout units interbedded with PDC and dilute-PDC deposits (Self and Rampino, 1981; Figure 3), some of which contain charcoal aligned east-west (Figure 6b) exist below the first lithic lag breccia (Unit C; Figure 6c). Unit D overlies this, and consists of massive PDC deposits (Mandeville et al., 1996; Self and Rampino, 1981; Figure 3) (Figure 6c). Figure 7 shows the logs from each locality cross-correlated by unit.

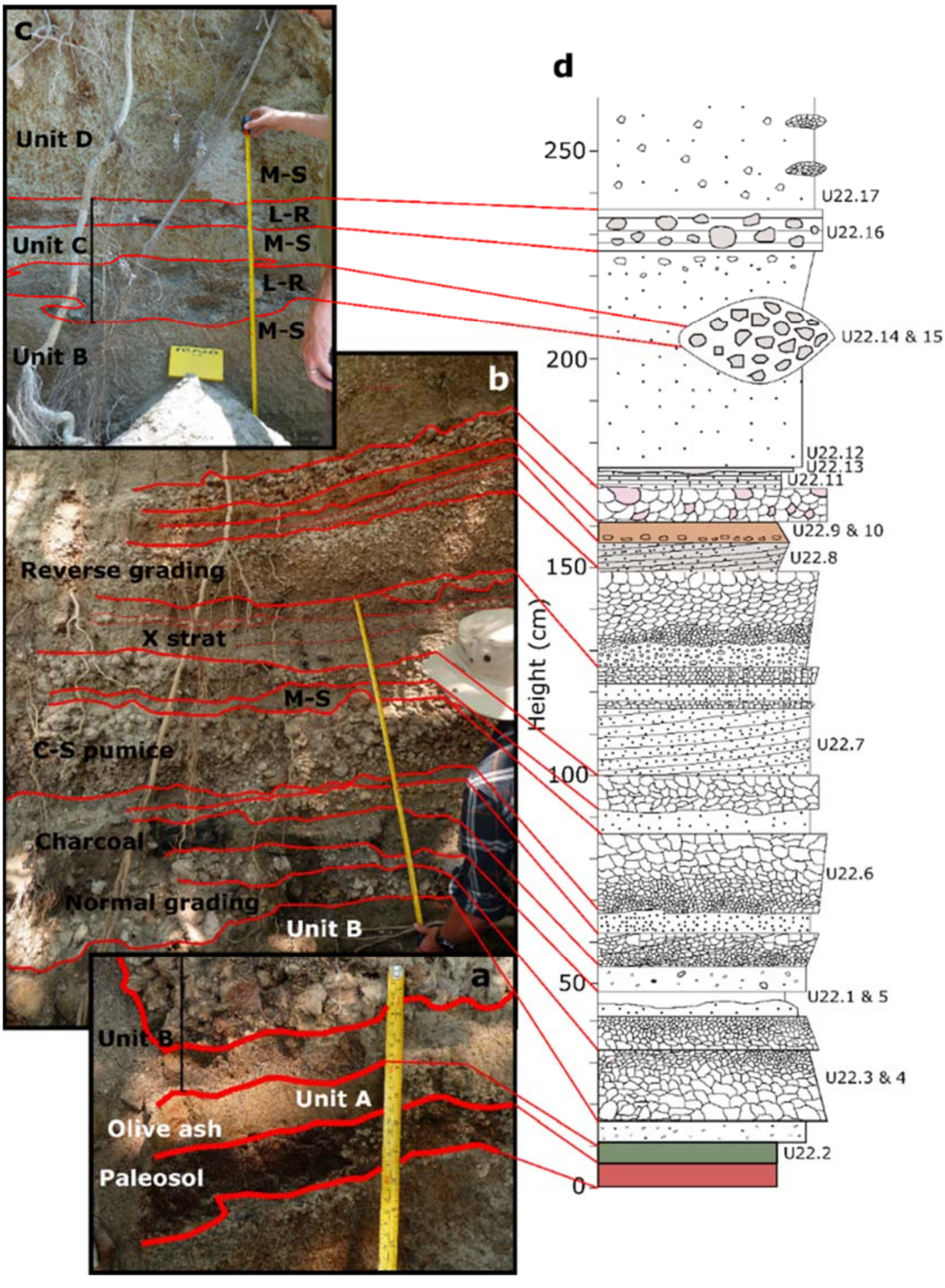

Figure 6: These photos were taken at locality U22 and are identified from the deposit base upwards (E. Rakata; location shown in figure 1). Panel (a) shows Unit A at the base of the sequence, (b) shows Unit B, (c) shows Units C and D, and (d) shows the cross correlated straigraphic log, with sample numbers down the right-hand side. C-S stands for clast-supported, X-strat for cross-stratification, M-S for matrix-supported and L-R for lithic-rich.

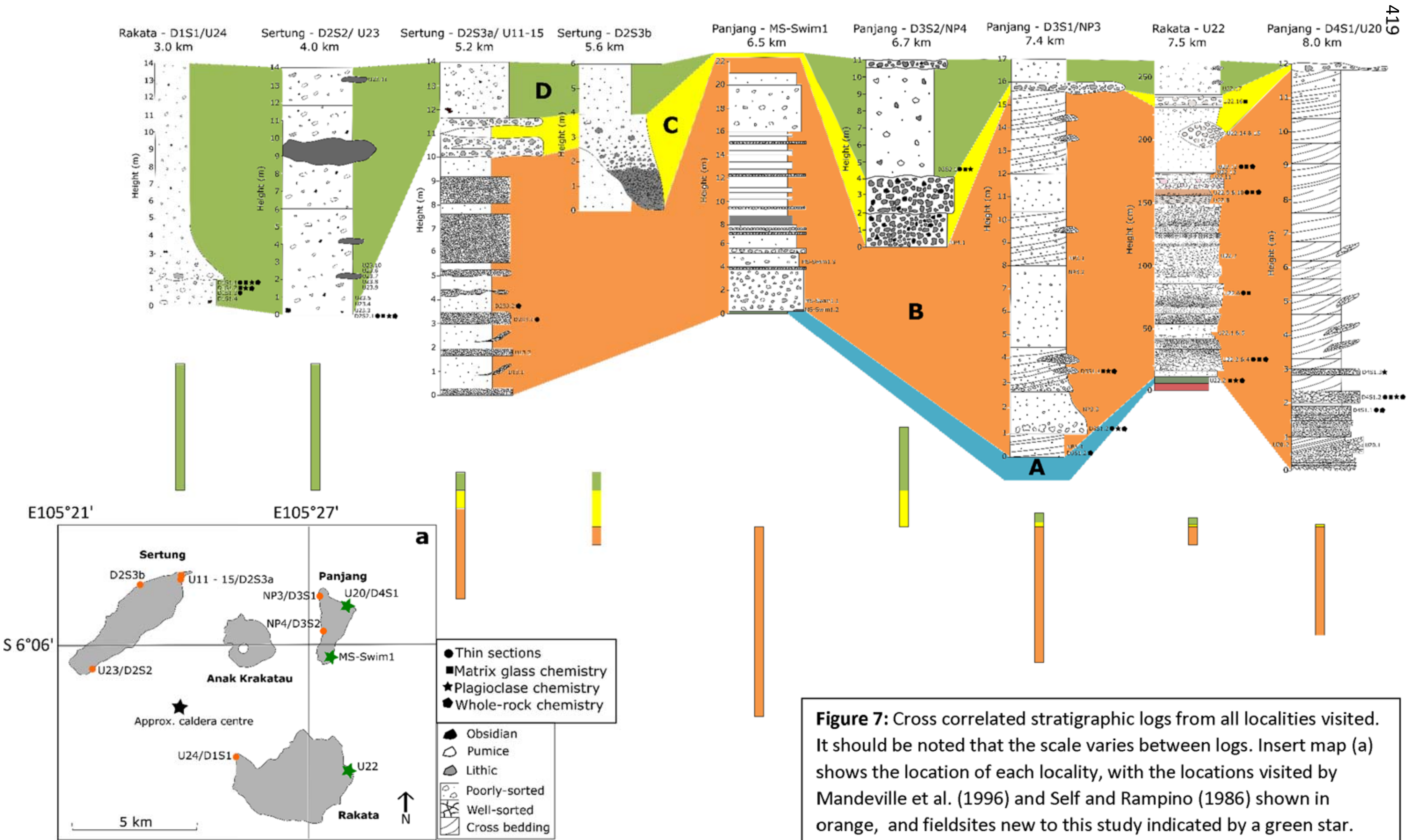

Figure 7: Cross correlated stratigraphic logs from all localities visited. It should be noted that the scale varies between logs. Insert map (a) shows the location of each locality, with the locations visited by Mandeville et al. (1996) and Self and Rampino (1986) shown in orange, and fieldsites new to this study indicated by a green star. Letters represent the discussed units, with A corresponding to blue, B to orange, C to yellow and D to green. Bars below logs represent the relative thicknesses of each unit. Symbols by sample numbers represent thin sections and chemical analyses. Distance above log is from the assumed caldera centre, taken from Deplus et al., (1995).

The spatial distribution and thicknesses of the PDC deposits also change through the stratigraphic sequence (Figure 8). Unit B is thickest to the north east, with approximately 20 m of exposure (Figure 8a). The deposition of Unit C appears to be more evenly distributed around the main island (Figure 8b), whereas Unit D is thickest in the south west (14 m; Figure 8c), rather than north, which was reported by Self and Rampino (1981). It should be noted that these thicknesses are based on limited exposure, and there are only two localities (MS-Swim1; south Panjang and U22; east Rakata) for which it was possible to observe the base of this sequence. This will lead to underestimates of unit thickness. Self and Rampino (1981) also noted a lack of fall deposits in the south west, which was also observed in this study.

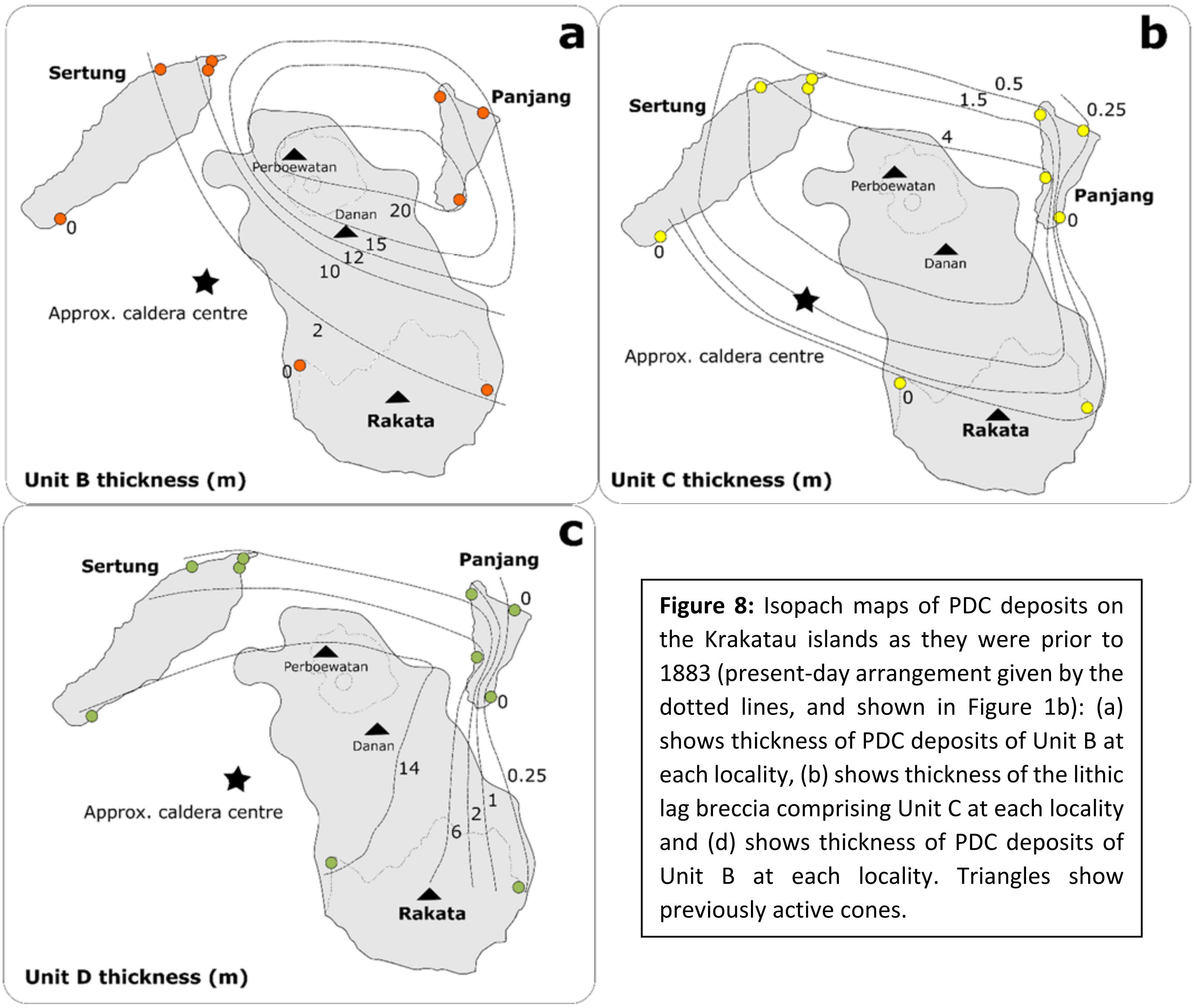

Figure 8: Isopach maps of PDC deposits on the Krakatau islands as they were prior to 1883 (present-day arrangement given by the dotted lines, and shown in Figure 1b): (a) shows thickness of PDC deposits of Unit B at each locality, (b) shows thickness of the lithic lag breccia comprising Unit C at each locality and (d) shows thickness of PDC deposits of Unit B at each locality. Triangles show previously active cones.

4.2 Vesicularity and crystallinity

Both crystallinity and porosity of juvenile clasts increase up the stratigraphic sequence. Unit A (n = 1) is comprised of poorly-vesicular ash aggregates, with crystallinity (on a vesicle-free (VF)/porosity-free basis) at 5 %. In Unit B (n = 7), vesicularity of pumice ranges from 40 – 65 %, with a mean value of 55 %. Crystallinity (VF) ranges from 5 – 15 %. Unit C (n = 1) pumice has a vesicularity of approximately 65 %, with crystallinity (VF) at 10 %. Pumice from Unit D (n = 3) has a vesicularity of 65 - 70 %, with crystallinity (VF), ranging from 15 – 25 %. In Mandeville et al. (1998), vesicularity ranges from 57 – 70 vol%, with a mean of 62 vol%, with all samples appearing to correlate with Unit B in this study. Vesicularity estimates are lower than those provided by Mandeville at al. (1998), and thus values reported in this study are likely to be underestimates due to plane of section effects and image resolution, however there is no reason to suppose that they would not be internally consistent.

4.3 XRF whole-rock

All XRF data can be found in Analytical Data 2 in the dataset Madden-Nadeau (2020). A Total Alkali and Silica diagram, along with Harker diagrams, for the 1883 stratigraphy is shown in Figure 9 (diamond symbols). Whole-rock SiO_2 ranges from 65.20 to 69.48 wt%. There is a negative correlation between total alkalis and silica. However, there is no discernible systematic correlation with stratigraphic height for all major and minor elements. Unit A appears to have higher FeO than the following units. It should be noted that the results presented here for whole-rock of 1883 pumice have a higher % total alkalis than previously reported, which is likely to be as a result of alteration, particularly as there is a correlation between SiO_2 and LOI (Supplementary Material 10).

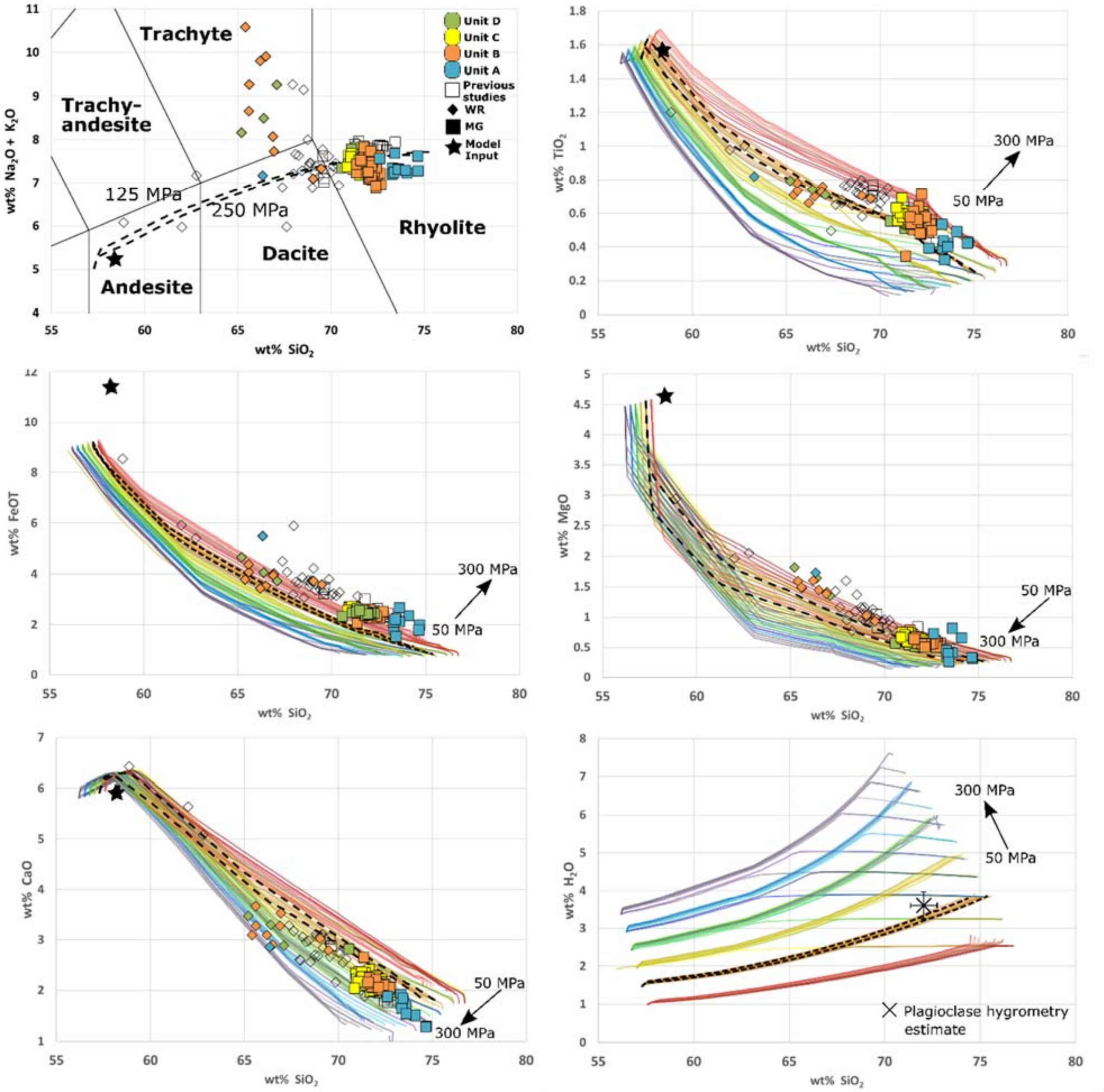

Figure 9: Total alkali and silica diagram (Le Bas et al., 1986) and Harker diagrams showing 1883 samples analysed in this study, with key in stratigraphic order, and colours denoting the different stratigraphic units, as presented in Figure 7. Diamonds indicate whole-rock (WR) and squares matrix glass (MG) data all of which is normalised to 100 % anhydrous totals. Data from previous studies (Oba et al., 1982; Self 1992; Mandeville et al., 1996a; Turner and Foden 2001; and Gardner et al., 2013) are presented with black outline and no fill. Liquid lines of decent are shown, modelled isobarically on Rhyolite-

MELTS. Red lines were modelled with initial H_2O contents of 1 wt%, orange 1.5 wt%, yellow 2 wt%, green 2.5 wt%, blue 3 wt% and purple 3.5 wt%. The dotted lines were modelled at 125 MPa and 250 MPa, with an initial H_2O content of 1.5 wt%. The input composition is indicated by the star (Darhen et al. 2012) and is from Anak Krakatau. Arrows indicate direction of increasing pressure from 50 to 300 MPa within the same initial water content (same colour). The cross indicates H_2O content of the average melt composition in units B to D, as modelled using plagioclase hygrometry (Water and Lange 2015) using the average temperature generated by Fe/Ti oxide thermometry (914 °C). Standard error of 0.35 wt% is indicated by the error bar, along with 2 σ of the average SiO_2 content. Inflection points on H_2O/SiO_2 plot where the lines flatten represent water saturation of the melt at the corresponding pressure.

4.4 Phenocryst chemistry

4.4.1 Plagioclase

Plagioclase is the dominant phenocryst phase in pumice clasts throughout the 1883 eruption stratigraphy. Zoning in plagioclase is complex, with a similar range of textures and compositions observed across stratigraphic units B to D, with crystal zoning profiles varying greatly between crystals (Figure 10). The total range of anorthite (An = molar Ca/(Ca+Na)) compositions present across all sampled plagioclase phenocryst cores, ranges from An_{31} to An_{90} (mean An_{54}; 81 analysed crystals). Phenocrysts also have a wide range in rim compositions: An_{40} to An_{65} (mean An_{49}; 64 analysed crystals) (Figure 10). Resorption textures are very common (e.g., Figure 10a), with some crystals having patchy cores and/or zones (~ 30 %; e.g. figure 10b). Both normal (~ 35 % of rims) and reverse zoning (~ 60 % of rims) are also common at various stages in plagioclase crystallisation histories, with ~ 5 % of crystals showing no zoning at all. Crystal chemistry does not converge towards a single anorthite composition. A high anorthite (>An_{70}) core is observed in ~ 20 % of phenocrysts.

For the majority of phenocrysts analysed for trace elements (n = 14; archive samples), there is an overall positive correlation between Fe and Anorthite (Figure 12). There is a positive correlation between Ti and An where $An_{<60}$, whereas for $An_{>60}$ Ti has a negative correlation with An. Mg has a similar overall trend to Ti, however these correlations are weaker, with more scatter. There is a negative correlation between Sr and An.

Two crystals, both picked from archive samples, are distinct from these observed trends. Phenocryst #07_08 has higher Fe, Mg, and Sr (Figure 12) than the other phenocrysts. Plagioclase #72_05 is also anomalous, with higher Mg and Fe. Both phenocrysts have similar zoning patterns: they both have a high An patchy core (An_{80} and An_{76}, respectively), followed by a mantle that contains fine oscillatory zones (Figure 13). The rim composition for both crystals is An_{58}. All analytical data for plagioclase phenocrysts, and accompanying BSE images, can be found in Analytical Data 3 – 11 in the dataset Madden-Nadeau (2020).

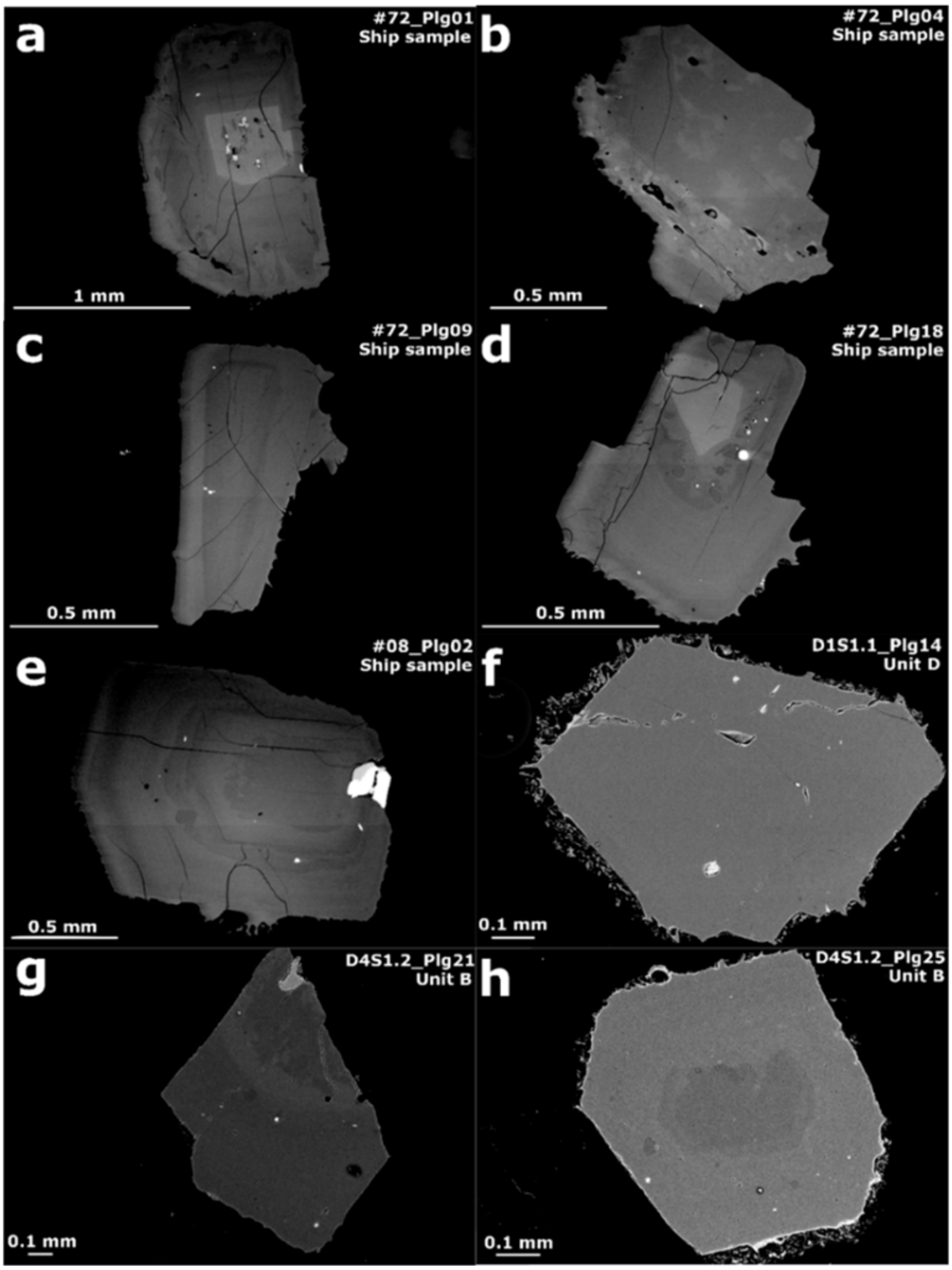

Figure 10: BSE images of a selection of plagioclase phenocrysts. Plagioclase (a) has a high anorthite core (indicated by the higher backscatter brightness), oscillatory zoning and some resorption textures; (b) has a patchy core, followed by a patchy zone; (c) has a single reverse zone between core and mantle; (d) has a high An core, followed by a patchy zone; (e) shows oscillatory zoning with a low anorthite core; (f) appears largely unzoned (g) a crystal fragment that has a patchy core followed by a reverse zone; and (h) has a low An core, followed by a reabsorbed zone before a higher anorthite mantle.

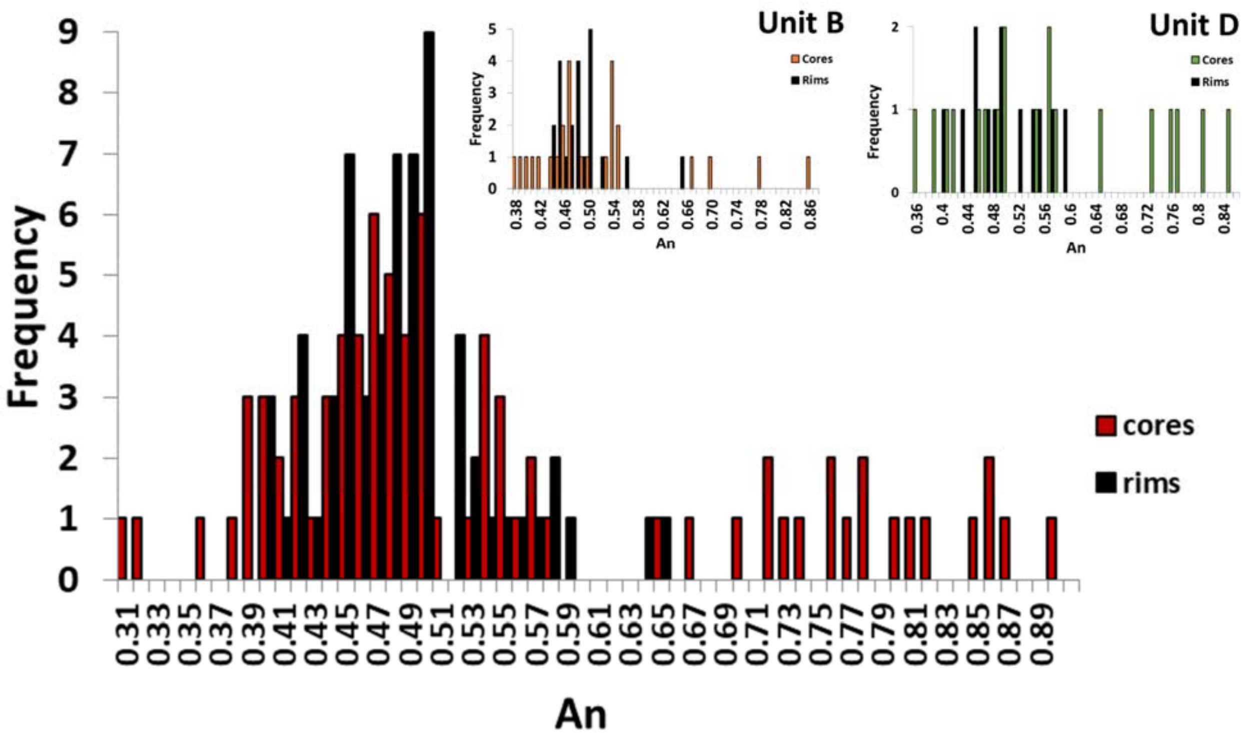

Figure 11: Histogram in red showing the frequency of core and rim compositions in anorthite for plagioclase phenocrysts; 83 individual crystals were used to create this histogram, taken from the 3 archived BGS samples, as well as 3 samples each from Units B and D. The two inserted histograms show distributions of anorthite compositions for Unit B and D individually, which are similar to the overall trend. It should be noted that there will be some error in crystal core compositions as a result of plane of section effects. Not all crystals had both viable core and rim analyses.

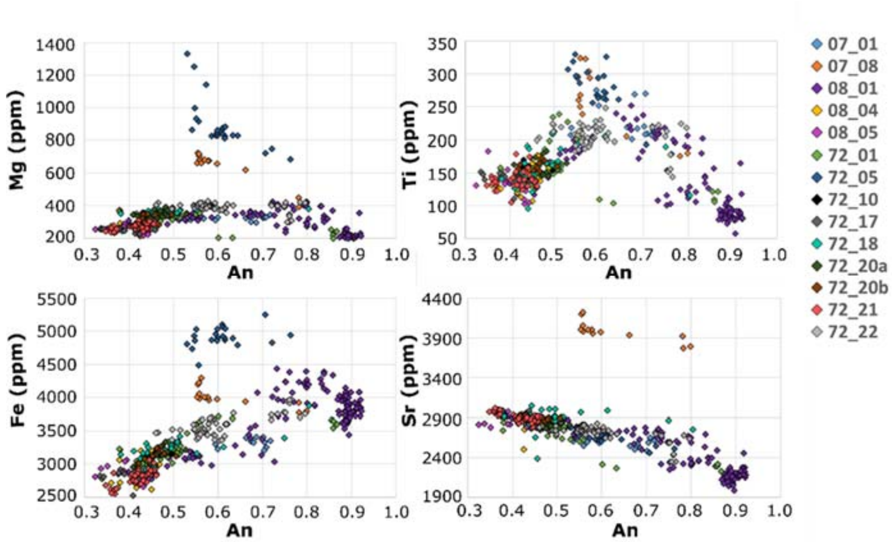

Figure 12: Trace elements plotted against anorthite content for plagioclase phenocryst traverses, picked from the archived BGS samples collected in August 1883. Data for each individual crystal is denoted by a different colour, and can be found in Analytical Data 3(a) and (h); 4(a), (c) and (d); and 5(a) - (c), (h), (m) - (r) in the dataset Madden-Nadeau (2020).

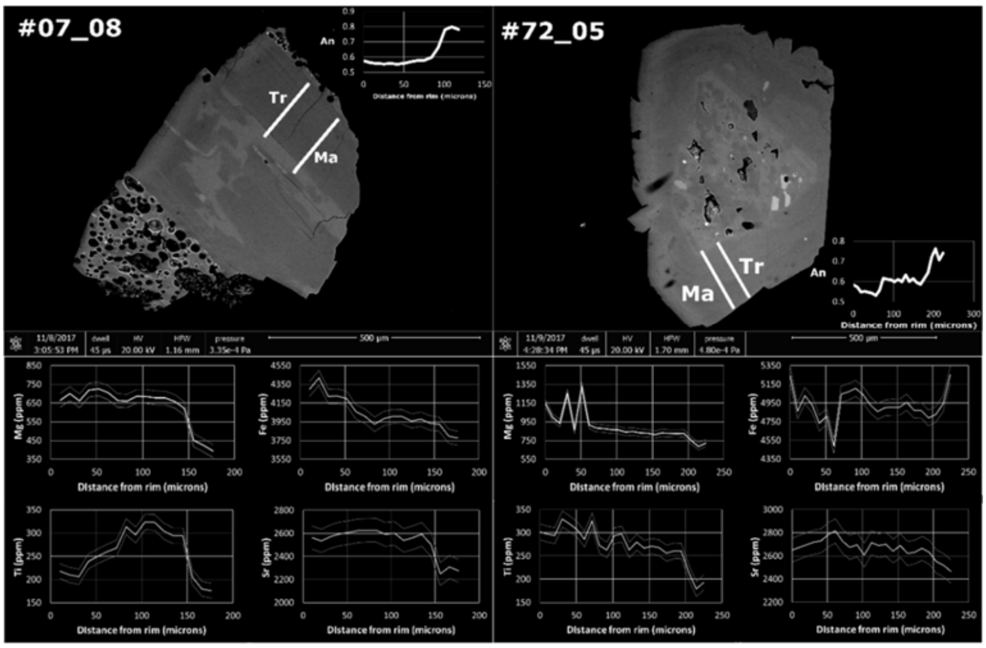

Figure 13: BSE images of two plagioclase phenocrysts from the archived BGS samples accompanied with their with trace element profiles. The major element profiles are denoted by Ma, with the trace element profiles Tr on the BSE images. Uncertainty (1 σ) is given by the light grey lines on trace element profiles.

4.4.2 Pyroxene and Fe-Ti oxides

Pyroxene phenocrysts were picked from the archived BGS ash samples, collected at the time of the eruption. Orthopyroxene rims and cores range in Mg# from 0.67 to 0.72 ($n = 22$, $\sigma = 0.1$), whilst the range for clinopyroxene is 0.73 to 0.77 ($n = 23$, $\sigma = 0.1$). Pyroxene phenocrysts are largely unzoned in the major elements. All data for pyroxene phenocrysts can be found in Analytical Data 12 – 14 in the dataset Madden-Nadeau (2020).

Fe-Ti oxides ($n = 419$) partially included in pyroxene rims were also analysed from the archived BGS samples, as well as from units B to D in the stratigraphy; they are magnetite and ilmenite. All chemical data for Fe-Ti oxides can be found in Analytical Data 15 in the dataset Madden-Nadeau (2020).

4.5 Matrix glass

Matrix glass data normalised to 100 % anhydrous compositions are plotted in Figs. 8 (Major elements) and 14 (zoomed in TAS), with full data table in Analytical Data 16 the dataset Madden-Nadeau (2020). Matrix glasses from Unit A are distinct, and more evolved than the rest of the proximal 1883 sequence, with SiO_2 ranging from 72.6 to 74.7 wt%. The data for Units B, C and D overlap, with a broad trend towards marginally less evolved compositions, showing a slight decrease in silica content alongside a reduced total-alkali compositional range, moving up the sequence (figure 14). SiO_2 for Unit B glasses range from 71.4 to 72.7 wt%, Unit C from 70.9 to 72.3 wt%, with Unit D ranging from 70.6 to 72.3 wt%. For each sample, this dataset encompasses analyses on at least two glass clasts picked from multiple crushed pumices, except for D1S1.2, where the only viable analyses came from the same clast.

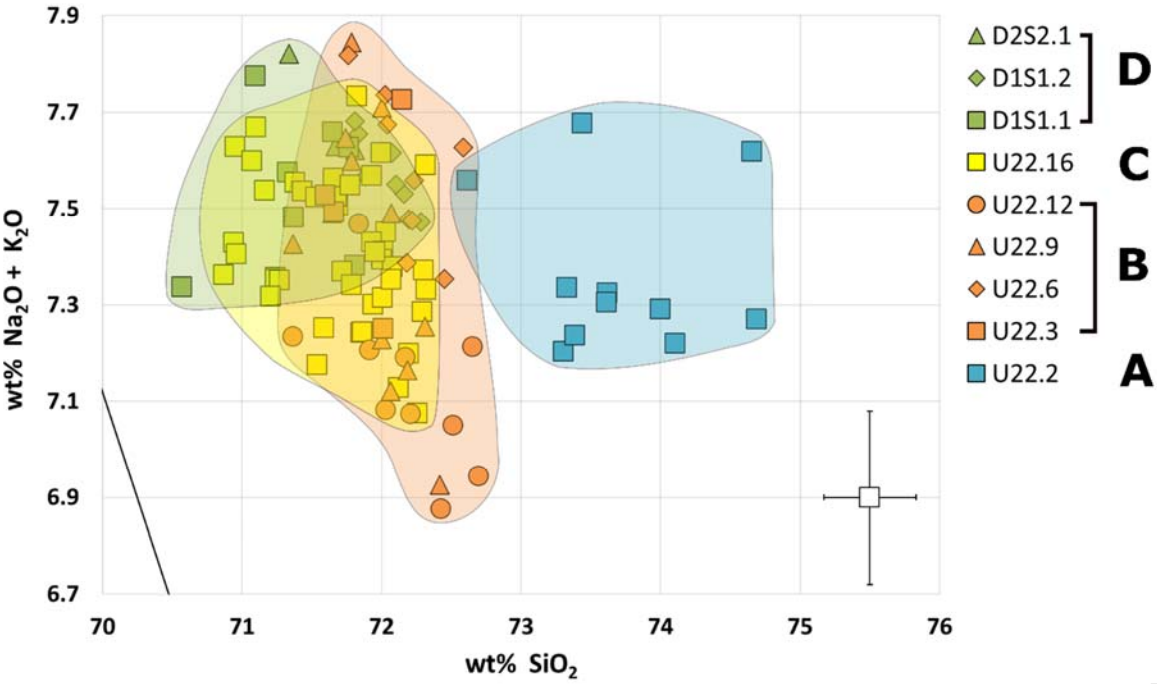

Figure 14: Close up of matrix glass data shown in Figure 9 on a total alkali and silica diagram (Le Bas et al., 1986). Colours of symbols and transparent areas correspond to stratigraphic units: A = blue, B = orange, C = yellow and D = green, as in Figure 6. Each symbol represents a separate sample, with the key in stratigraphic order. Unit A is more evolved than, and distinct from, Units B to D. Average error is given to 1 σ.

4.6 Thermobarometry

4.6.1 Fe-Ti oxides

Magnetite and ilmenite compositions were inputted into the model for Fe^{2+}-Mg exchange outlined in Ghiorso and Evans (2008) to produce temperature and fO_2 estimates. The Fe-Ti oxide pairs were tested for equilibrium using the Mg-Mn equilibrium line (Bacon and Hirchsmann, 1988). Fe-Ti oxides are likely to yield the last equilibration temperature before quenching (Rutherford and Devine, 1988; Geschwind and Rutherford, 1992; Lindsley and Frost, 1992).

The temperature range for all Fe-Ti oxide pairs (n = 71; 24 touching, 47 partially included within the same pyroxene phenocryst and 7 other pairs; chemical data in Analytical Data 15; dataset Madden-Nadeau 2020) was 890 to 935 ^{o}C, with a mean value of 914 ^{o}C. The range of temperatures generated for the 24 touching Fe/Ti oxide pairs is between 891 and 935 ^{o}C, with an average of 913 ^{o}C. The oxygen fugacity (fO_2) range is + 0.6 to 0.85 log units relative to nickel-nickel-oxide buffer, with a mean of 0.77. The entire range of values for fO_2 is seen within the data set for the 24 touching pairs, with a marginally lower average of 0.74. The temperatures and fO_2 of units B, C and D all show considerable overlap, with unit D extending to marginally higher temperatures (890 to 935 ^{o}C) than unit B (893 to 927 ^{o}C). A temperature fO_2 plot can be found in Supplementary Material 11. It should once again be noted that these temperatures represent only the final equilibration temperature, and thus do not reflect any conditions prior to this.

4.6.2 Plagioclase hygrometer

Pre-eruptive dissolved water content of the melt for samples from units B and D are estimated using the hygrometer outlined by Waters and Lange (2015). Anorthite content of plagioclase rims and matrix glass data (n = 49), as well as the mean temperature Fe/Ti oxide thermometry (914 ^{o}C) determined a mean H_2O content of 3.6 wt % (figure 9). Using the entire range of temperatures generated by the Fe/Ti oxide thermometry (890 to 935 ^{o}C), gives a range of 3.0 to 4.2 wt%. This is consistent over 100 to 250 MPa. There was no difference between the two units. It should be noted that these will be final H_2O contents, owing to the nature of the temperature estimates inputted, and thus do not reflect the entire range of conditions experienced by plagioclase phenocrysts throughout their crystallisation histories.

Equilibrium in plagioclase is difficult to test, owing to composition being a function of both temperature and H_2O content, however the range of plagioclase compositions for the chosen melt composition matches the data used to calibrate the hygrometer (Supplementary Material 12).

4.7 Rhyolite-MELTS modelling

Melt evolution was modelled using Rhyolite-MELTs (Gualda et al., 2012) (Figure 9). The starting composition is the most primitive composition (4.63 wt% MgO) from Anak Krakatau analysed by Dahren et al. (2012). Initial H_2O contents of 1 – 3.5 wt% H_2O were modelled isobarically, with pressure varied between runs (50 to 300 MPa; steps of 50 MPa). In all runs, temperature was dropped from 1200 to 700 °C in increments of 2 °C. The lines of descent that fit the best with the whole-rock and matrix glass compositions were modelled at an initial H_2O content of 1.5 wt%, and are between 125 and 250 MPa (Figure 9). The evolution of H_2O within the melt indicates that it is water-undersaturated prior to eruption under these conditions. Varying the initial water content has a much larger effect on the liquid line of descent than varying the pressure.

5 Discussion

5.1 Structure of plumbing system

An understanding of the structure of the magma plumbing system is key when assessing volcanic hazard (Edmonds, 2008). The lack of systematic change in either whole-rock major or trace element chemistry with stratigraphic height (Figure 15) is not consistent with the existence of a single chemically-zoned magma reservoir at shallow depths, as suggested previously for the 1883 eruption by Mandeville et al. (1996a) and Gardner et al., (2013), or such as that hypothesised for similarly large magnitude, explosive eruptions, such as the Green Tuff, Pantelleria (Williams et al., 2014) and the Bishop Tuff (Hildreth and Wilson 2007).

The magmatic storage conditions immediately prior to eruption have been assessed previously (e.g. Mandeville et al., 1996a), however updated temperature, pressure and water estimates are provided here. Temperatures were reported by Mandeville et al., (1996a) for homogenous rhyodacite (880-890 °C), dacite (890-913 °C), and andesite (980-1000 °C) found within the 1883 tephra, and are suggested to be evidence for a stratified magma reservoir. However, the lower silica components are estimated to form only a minor component of the erupted volume (6 %), and there is no evidence that their frequency varies with stratigraphic height. In addition, there is no evidence for these lower Si compositions as a juvenile melt component in the samples analysed in this study. This study finds the temperature estimates provided by Fe/Ti oxides by the updated model provided by Ghiorso and Evans (2008) show no variation with stratigraphic height, with an average temperature of 914 °C. These estimates also show a narrower range than those previously reported, at 890 to 935 °C. These differences could be as a result of using the updated model, as well as the fact that some clasts used to provide temperature estimates in Mandeville et al. (1996a) represent a volumetrically minor component of the magma (e.g. the andesite clasts are estimated as representing 1% of the erupted volume).

The average estimate of 3.6 wt% H_2O provided in this study, agrees with those previously reported from LOI of glass analyses (4 +/- 0.5 wt%; Mandeville et al., 1996a). Pressure estimates have been provided by the Rhyolite-MELTS modelling, at 125 – 250 MPa, equivalent to approximately 5 to 10 km within the crust, which agrees with depth estimates for the shallow system, estimated using plagioclase melt barometry by Mandeville et al. (1996a), of 5 – 8 km.

The matrix glass comprising Unit A is chemically distinct and more evolved than the rest of the sequence (Figure 15), indicating the presence of a more silicic, likely shallower magma body that was erupted first. Unit A appears to have marginally higher Fe, Ti and Mg for whole-rock chemistry than subsequent units, along with lower Ca, Na and K, which could suggest that this melt crystallised slightly different mineral modalities, e.g., higher Fe-oxide minerals relative to plagioclase.

Crystallisation of plagioclase and two pyroxenes, in the shallow system, is estimated at approximately 4 and 8 km respectively for Anak Krakatau (Dahren et al. 2012). Dahren et al. (2012) inferred that the magmatic plumbing system had not changed significantly since 1883, as a result of lithological controls on reservoir formation; these depths are corroborated by seismic tomography data (Jaxybulatov et al., 2011; Harajono et al., 1989). Pyroxene phenocrysts lack strong zoning, which would either suggest consistent magmatic conditions, or that the crystals were resident long enough for diffusion to smooth out their crystallisation histories. Plagioclase phenocrysts, on the other hand, have complex growth histories, with zoning patterns that vary from crystal to crystal, including a small number of crystals (5 %) that are completely unzoned (Figures 11 and 12). In addition, crystal rims are not consistent, spanning a range from An_{41} to An_{61} (Figure 12). This suggests that the plagioclase phenocryst population crystallised across a range of pressure and temperature conditions, if not different melt compositions.

Diffusion of Mg is faster in plagioclase than in pyroxene, therefore the presence of Mg zoning in plagioclase but not pyroxene suggests this is not controlled by time-dependent diffusion, assuming both phases evolved in the same magma. To illustrate this a first order estimate of diffusion timescales for both phases is provided using the following equation:

x = sqrt(Dt)

where x is the mean diffusion length, D is the diffusion coefficient and t is time. A zoning signature over a 10 micron distance would take on the order of centuries for diffusion in pyroxene at 900 °C to flatten any Mg variation, using the diffusion coefficient given by Schwandt et al. (1998) of 4.72×10^{-21} m^2/s. Mg variations are recorded in the zoning profiles in plagioclase phenocrysts (Figure 13), and when the above diffusion equation is applied to plagioclase, for the same temperature, over the same distance, using the Mg diffusion coefficient given by LaTourrette and Wasserburg (1998) of 7.19×10^{-18} m^2/s, the timescales are in the order of months to years. Therefore, both plagioclase and pyroxene phenocrysts could not have been resident in a hot magma for sufficient time to smooth the Mg profiles in the pyroxene population, as the Mg variations in plagioclase are retained. This implies that diffusion is unlikely to be the cause of the discrepancy in zoning complexity between the two crystal populations.

There are two plagioclase phenocrysts that have different trace element profiles to the other 14 crystals analysed (Figures 12 and 13). Phenocryst #07_08 has higher Fe, Mg and Sr for a given An content (Figure 12a, c and d). The Ti concentration for a given An is in a similar range for $An_{<60}$ relative to other crystals, indicating that this crystal is likely to have crystallised in lower temperature conditions, if not in an entirely different melt, as Ti contents in plagioclase are not sensitive to temperature changes (Ginibre et al. 2002). Plagioclase #72_05 has elevated Fe and Mg contents. Sr and Ti contents are consistent with other crystals. Since Sr concentrations are not sensitive to melt composition (Wood and Blundy 1991), the elevation in the other elements can be explained if this phenocryst crystallised in a different reservoir. It is unlikely that these crystals are entirely xenocrystic, as they have very similar Ti contents to the rest of the crystal population, indicating they are likely derived from the same source melt. The existence of these phenocrysts can therefore be explained by multiple melt-rich regions within a single, or multiple reservoirs. The existence of multiple smaller melt lenses is consistent with a reduction in seismic travel speeds within the shallow system of Anak

Krakatau, with a lack of evidence for a long-lived large melt-rich reservoir (Gardner et al., 2013; Jaxybulatov et al., 2011; Harajono et al., 1989).

The matrix glass SiO_2 contents for Units B to D (Figure 14) display only subtle compositional differences with stratigraphic height. Whilst Unit B spans the entire range of total alkali compositions present, Units C and D occupy a narrower and less evolved (less silicic and higher alkalis) compositional range, potentially suggesting that the latter phases of the eruption tapped a more homogenous, slightly less evolved magma. The broad compositional consistency, however, means that the multiple melt-rich lenses are likely of similar bulk compositions. This suggests that the discrepancy in crystallisation histories recorded by plagioclase and pyroxene phenocrysts owes to the fact that plagioclase is far more sensitive to changing conditions, e.g. P_{H2O} (e.g., Mollo et al., 2011), and thus is more likely to record these fluctuations than pyroxene phenocrysts. In a system where melt composition is similar, but phenocrysts are crystallising under different conditions e.g. temperature, fO_2, P_{H2O}, plagioclase could record complex crystallisation histories, whilst pyroxene remain largely unzoned. It should be noted that this is not contradicted by the estimates provided for temperature and H_2O content, as these only represent the final pre-eruptive equilibration conditions.

The presence of some anorthite-rich (An_{70} to An_{92}) plagioclase cores likely indicates the presence of a deeper, more mafic reservoir feeding the shallow system. This corroborates estimates of plagioclase crystallisation depths of ca. 25 km obtained by Mandeville et al. (1996) for the 1883 eruption, and Dahren et al. (2012) for the Anak Krakatau system. The range of plagioclase core compositions (An_{70} to An_{92}) indicates that these cores grew under differing conditions (e.g. fO_2, T, P, H_2O content), possibly in multiple melt-rich pockets within the deeper system. Sieve textures in high anorthite cores, as well as strong resorption textures (Figure 13b), are consistent with decompression (Nelson and Montana 1992), potentially during extraction from this deeper reservoir, and subsequent mixing with magmas in the shallow system. The lack of significant variation in whole-rock and matrix glass data can be explained if the magmas are all originally sourced from a similar host composition.

5.2 Role of pre-eruptive fractional crystallisation

Fractional crystallisation increases the SiO_2 content of the residual melt, whilst also enriching it in volatiles, with both factors making an eruption more likely, and also potentially more explosive (Blake 1984). However, the importance of this process varies greatly between volcanoes, with other processes such as magma mixing often cited as eruption triggers (e.g., Sparks et al., 1977). It is thus important to discuss the role of fractional crystallisation in the magmatic system prior to the 1883 eruption of Krakatau.

Mandeville et al. (1996) conclude that fractional crystallisation must be the dominant process in the plumbing system beneath Krakatau prior to its 1883 eruption. This is because there is only a very small amount of mixed pumice within the stratigraphy, and they found that reverse zoning was not prevalent or consistent enough in the phenocryst population, meaning that the eruption was likely not triggered by magma mixing.

The results of the Rhyolite-MELTS modelling (Figure 9) show that it is possible to get from a more primitive Anak Krakatau composition to the major elements and estimated water content (using plagioclase hygrometry; Waters and Lange 2015) of the 1883 silicic melt by only invoking the process of fractional crystallisation, when using a starting H_2O content of 1.5 wt%. The model best fits pressures between 125 and 250 MPa. Small discrepancies between the model and natural samples may be as a result of the system not being entirely isobaric. The fact that we can generate compositions similar to the 1883 eruptive products, from a basaltic andesite host (from recent products from Anak Krakatau), supports the notion that volatile saturation could be achieved through crystallisation alone. Eruptions of silica-rich magma bodies at < 300 MPa can be internally triggered by fractional crystallisation, without efficient degassing (Tramontano et al., 2017).

However, looking at the modelled evolution of H_2O in Figure 9, and given that the natural data best fit with modelled evolution of 1.5% initial water content at pressures of 125 – 250 MPa, it is likely that this reservoir did not reach water saturation prior to eruption. This is supported using VolatileCalc (Newman and Lowenstern 2002), which estimates H_2O saturation at a minimum of ~95 MPa, with inputs of 3.6 wt% H_2O at a temperature of 914 ^oC. The volcanic system was, however, approaching volatile saturation, and eruption in the near future in any case. Thus fractional crystallisation may have helped to prime the magmatic system for eruption by another trigger.

Normal zoning is a common feature in plagioclase phenocrysts, and accounts for ~35 % of all rims, supporting an interpretation that a proportion of phenocrysts were growing under stable conditions immediately prior to eruption, with melt evolution driven by fractional crystallisation. In addition, the positive overall correlation between Fe and anorthite in plagioclase phenocrysts found in Units B to D (Figure 12), is consistent with experiments and petrological studies that show similar trends as a melt evolves (Bindeman et al. 1998; Ginibre et al. 2002; Cassidy et al. 2015). The partitioning of Ti in plagioclase at $An_{<60}$ appears to be crystal controlled, as there is a positive correlation between Ti and An, whereas for $An_{>60}$, Ti has a negative correlation with anorthite (Figure 12b). Therefore plagioclase growth where $An_{>60}$, is likely to be controlled by evolution of the melt through crystallisation (Bindeman et al. 1998; Ginibre et al. 2002; Cassidy et al. 2015). The positive correlation between An and Mg for $An_{<60}$ (Figure 11) is again recording this same process. The negative correlation of Mg with $An_{>60}$, however, is neither crystal controlled, nor compatible with differentiation, and thus may be as a result of changing conditions, such as temperature, water content or pressure

(Bindeman et al., 1998; Ginibre et al., 2002; Cassidy et al., 2016). One explanation might be that the partitioning of Mg between melt and plagioclase at higher anorthite contents was the result of another process, such as melt extraction from a deeper reservoir, and subsequent mixing. The negative correlation between Sr and An means that Sr partitioning is likely to be crystal controlled (Wood and Blundy 1991; Ginibre et al., 2002).

Overall, crystallisation of the melt appears to be an important process of pre-eruptive magma genesis, based on normal zoning with phenocrysts, as well as trace element compositions. The Rhyolite-MELTS modelling also shows that no other internal processes need to be invoked to reach the composition of the 1883 magmas from basaltic andesite compositions produced within the same system. This is consistent with whole-rock Sr isotope analyses on more recent Anak Krakatau samples, which suggest that fractional crystallisation dominates the current system (Gardner et al., 2013).

5.3 Role of pre-eruptive magma mixing

Recharge of magma reservoirs and subsequent magma mixing are often cited to be eruptive triggers, however it has been shown through Rhyolite-MELTS modelling that this process need not be invoked in order to generate magmas of 1883 composition. Mandeville et al. (1996) rule magma mixing out as a trigger for the 1883 eruption, based on a lack of reverse zoning in their study, and a low abundance of mixed pumices. However, 60% of plagioclase phenocrysts in this study show reverse zoning at the rim, a result likely obtained as a result of investigating crystal zoning at a much higher spatial resolution. It is important therefore to discuss the role that magma mixing had prior to the 1883 eruption of Krakatau.

The high proportion of reverse zoned rims indicate a shift in P, T and/or H_2O conditions, and/or compositional changes for the majority of plagioclase crystals prior to eruption. However, plagioclase phenocryst rim chemistry does not converge on a single composition, which might be expected if large-scale mixing with a magma of significantly different composition (occurring most frequently as mafic recharge; Sparks et al., 1977) triggered the 1883 eruption. In addition, the volume of visually mingled pumice is small (Mandeville et al., 1996a), and is not observed in Units A – C of the stratigraphy. In any case, it would also be expected that compositional differences would be found in the matrix glass of these mingled pumices, and none have been found (this study; Self 1992). Mafic enclaves are also entirely absent within the stratigraphy. It should be noted that although Stehn (1929) reports some ash of mafic composition collected during the precursory eruptive phase, evidence of this ash was not observed on either field campaign, suggesting this is a volumetrically minor component, possibly similar to the andesite glass (~1 %) reported by Mandeville et al., (1996a).

Syn-eruptive mixing would account for the wide range in plagioclase rim compositions, as they would not have had time to equilibrate with the new host melt. The narrow range in matrix glass composition (Figure 13) and bulk chemistry (Figure 9), suggests that these melt lenses therefore likely had similar chemistries, meaning that any small differences could be smoothed out via mixing. It is therefore most likely that different melt lenses within the shallow system coalesced and mixed syn-eruptively as a result of system restructuring. In this case magma mixing would be considered a consequence of magma body destabilisation during eruption, rather than an eruptive trigger (e.g., Christopher et al., 2015); this has been invoked as an explanation for homogeneity in pyroclasts coexisting with complex phenocryst zoning for similar crystal-poor caldera systems (Cashman and Giordano 2014).

5.4 Eruptive progression

A schematic diagram illustrating the proposed evolution of the magmatic system and how this links with the eruptive progression is shown in Figure 15. Unit A (Figure 4a) is comprised of a green ash aggregate fallout deposit at the base of stratigraphy, which is distinct in its chemistry, being more evolved than the eruptive material that follows (Figure 8 and 13). Unit A therefore likely represents the sub-Plinian May phase of the 1883 eruption of Krakatau, erupted from a more-evolved, shallow reservoir (Mandeville et al., 1996b). This is supported by reported observations of a maximum of 50 cm of green ash at the coast in June (Symons et al. 1888). This eruption was likely not triggered by mafic recharge, owing to the lack of evidence (discussed in section 5.3), e.g., abundant banded pumices lack of consistent reverse zoning at the crystal rims, and the fact that the Rhyolite-MELTs modelling predicts only crystallisation needs to be invoked to produce the 1883 eruptive compositions. However, Rhyolite-MELTS simulations predict that the melt was water undersaturated, and so the eruption was unlikely to be triggered by “second-boiling” either.

As suggested previously by Mandeville et al., (1996b), the fact that Unit A is comprised of ash-aggregates could indicate that the May 1883 activity was phreatomagmatic. This interpretation is consistent with historical accounts made by inhabitants of the nearby island of Sebesi, who visited the main island of the Krakatau complex on 21st of May: “the earth burst open at their feet” on the beach, and this is confirmed the next day by European officials who travelled from Anjer. Their accounts follow: “near the beach, the earth was belching fire and smoke” (Furneaux 1964). According to these accounts, Krakatau was erupting close to the coast at this time, making magmatic interaction with seawater more likely. This is corroborated by reports from the ship Prins Hendrick, which passed close to Krakatau on 12th August: “I passed the island on the north side… the new opening of the crater... appeared to be a small hole, maybe 100 ft in diameter, only a few meters above sea level” (Macleod 1884). However, Ferzenaar, a visitor to the island in the day before, noted only distinctly subaerial vents prior to the climactic phase of the eruption.

There are periods in both early June and late July which have sparse historical records (Figure 2), and it is not known whether the activity was continuous. The volcano was attracting much less attention, and therefore it is likely at least that the eruptions were smaller, if not less frequent. It is thus difficult to know whether any activity after 27th May contributed significantly to the deposition of Unit A or not.

As discussed in the previous section (5.3), the wide range in plagioclase rim compositions, along with the lack of evidence for mafic recharge, suggests that, subsequent to the initiation of the May phase of the eruption, it is likely that adjacent reservoirs restructured, coalesced, and mixed as a result of stress changes. A reduction in the height of the summit of Perboewatan is reported by residents on the coast of Java on 24th June (Symons et al. 1888), whereas Ferzenaar, during a visit on 11th August, reported that Danan that had lost volume (Verbeek 1885; Figure 2). In either case, the destruction of part of the Krakatau island is one potential candidate for causing these downward propagating stress changes (e.g., Tarasewicz et al., 2012). A second possibility is that the emptying of the shallow, more silicic reservoir from May onwards may itself have caused, or contributed to, the stress changes that allowed for the restructuring of the shallow system.

Any scenario for magma body destabilisation occurred over ~ 2-3 months before the onset of the paroxysmal phase of the eruption. Unit B represents the onset of this climactic eruptive phase, comprising interbedded PDC and fallout units, and tree remains. The deposition of Unit B may have started as early as 22nd August (figure 2). Unit B is much thicker (up to 20 m) than Unit A (< 5 cm). Increasing magma flux throughout the deposits is evidenced by increased deposit thicknesses, with the increasing degree of fragmentation recorded in the increasing degree of vesiculation (Giordano and Cashman, 2014). The stress changes will have reduced the overburden on the shallow magmatic system, which may have allowed the magma to ascend faster, increasing the magma flux, and the explosivity of the eruption (Watt, 2019).

Deposition of the PDC deposits included within Unit B also appear to be thicker in the north east (Figure 8), suggesting that this was the dominant direction of travel. The north east direction of travel may be as a result of the summit of Danan (> 400 m) lying to the south, acting as a topographic barrier blocking PDC transport. Accounts from 23rd August corroborate this, with ash being reported in the north east in the straits of Sunda by ships such as the Princes Wihelmina (Macleod 1884), with heavy rains of pumice in the north in Lampong Bay on 26th August.

Massive PDCs comprise Unit D, overlying a lithic lag breccia termed Unit C. Unit D seems likely to emanate from the inferred caldera centre, with a dominant direction of travel towards the south west (Figure 8). This could indicate that the topographic barrier of the edifice Danan was removed in a partial collapse of the island, causing the formation of the lithic lag breccia observed in Unit C; after this removal, the massive PDCs comprising Unit D could travel more easily to the south west.

The thick, structureless PDC deposits emplaced as part of Unit D potentially correspond with the paroxysmal explosions, in the morning of 27th August 1883. At the top of Unit D, a lithic lag breccia is observed at locality D3S2/NP4 (Figure 5b), and at D2S2/U23 (Figure 5c) there are massive metre-scale blocks of jointed lava. These are very similar to the large, in that case, hyaloclastite lava blocks found towards the top of the Late Bronze Age (Minoan) eruptive sequence in Santorini (Druitt and Francaviglia 1992; Sparks and Wilson 1990). By analogy, these massive blocks may have been entrained during the final stage of caldera collapse, from the volcanic island. If this is the case, the high eruptive energy required to incorporate and transport such blocks means that this section of the stratigraphy potentially corresponds to the largest explosion, and most devastating tsunami, at 10 am on 27th August 1883. The rounded, irregular shapes of these blocks perhaps suggest ductile deformation during hot emplacement. This gives rise to another hypothesis for their formation: the lava blocks are juvenile, and were erupted concurrently with the pyroclastic material. This is supported by the fact that some of these lenses were very similar to obsidian clasts found within this unit, at least some of which are likely to be juvenile, owing to their frothy textures. However, other blocks are grey rather than black, and much duller in appearance; compositionally distinct lenses would be more consistent with them being entrained relics of the island, or a combination of entrained and juvenile material.

No textural evidence for phreatomagmatic activity was found in Unit D. This is contrary to what might be expected if the caldera collapse promoted magma-water interaction. However, there are records of ash falling as “rounded accretions” in Java after the main paroxysm (which we equate to Unit D, (Figure 2), which may provide evidence for magma interacting with water during or after caldera collapse. It may be that evidence for phreatomagmatism is simply not preserved in the stratigraphy.

The deposits from the 1883 Krakatau eruption are consistent with those observed in many caldera-forming eruptions, e.g., Bishop Tuff (Hildreth and Wilson 2007), Crater Lake (Bacon 1983; Kamata et al., 1993) and Santorini (Druitt et al., 2019). These eruptions commonly start with a Plinian plume, with the single vent widening through time and PDCs contributing to an increasing proportion of the erupted products. Caldera collapse then occurs when a critical volume of magma has been removed from the plumbing system beneath. The tapping of multiple melt batches has been documented for many crystal-poor caldera-forming eruptions, particularly in systems undergoing active extension, similar to Krakatau, e.g., the Snake River Plain (Ellis et al., 2010; Ellis and Wolff, 2012) and the Taupo Volcanic Zone (Brown et al., 1998; Charlier et al.,2003; Gravley et al., 2007; Wilson and Charlier, 2009; Bégué et al.,2014). In these cases, melt was stored in laterally (rather than vertically) extensive systems, with a consistent bulk chemistry between melt lenses (Cashman and Giordano 2014). Many caldera-forming eruptions are preceded by some form of precursory eruption, however the period of time between this and the climactic eruption is often poorly constrained (e.g., Allan et al., 2012; Cashman and Giordano 2014; Druitt et al., 2019). The 1883 eruption of Krakatau is unique in the sense that from direct observations we can say precisely when this precursory activity began (Unit A; 20th May 1883). This may be invaluable for monitoring volcanoes with a history of producing explosive caldera-forming eruptions, because it highlights the potential for a large event to follow a relatively moderate explosive eruption on a timescale of months. However, although a precursory Plinian eruption might increase the risk of a larger eruption, one does not always follow on from the other. Top-down factors, such as the removal of mass from the volcano edifice (discussed earlier in the section; 5.4), potentially have a role in triggering these devastating paroxysms. Therefore, it would also be useful to carefully monitor surface deformation and any significant losses of mass at Anak Krakatau, as well as other similar volcanic systems.

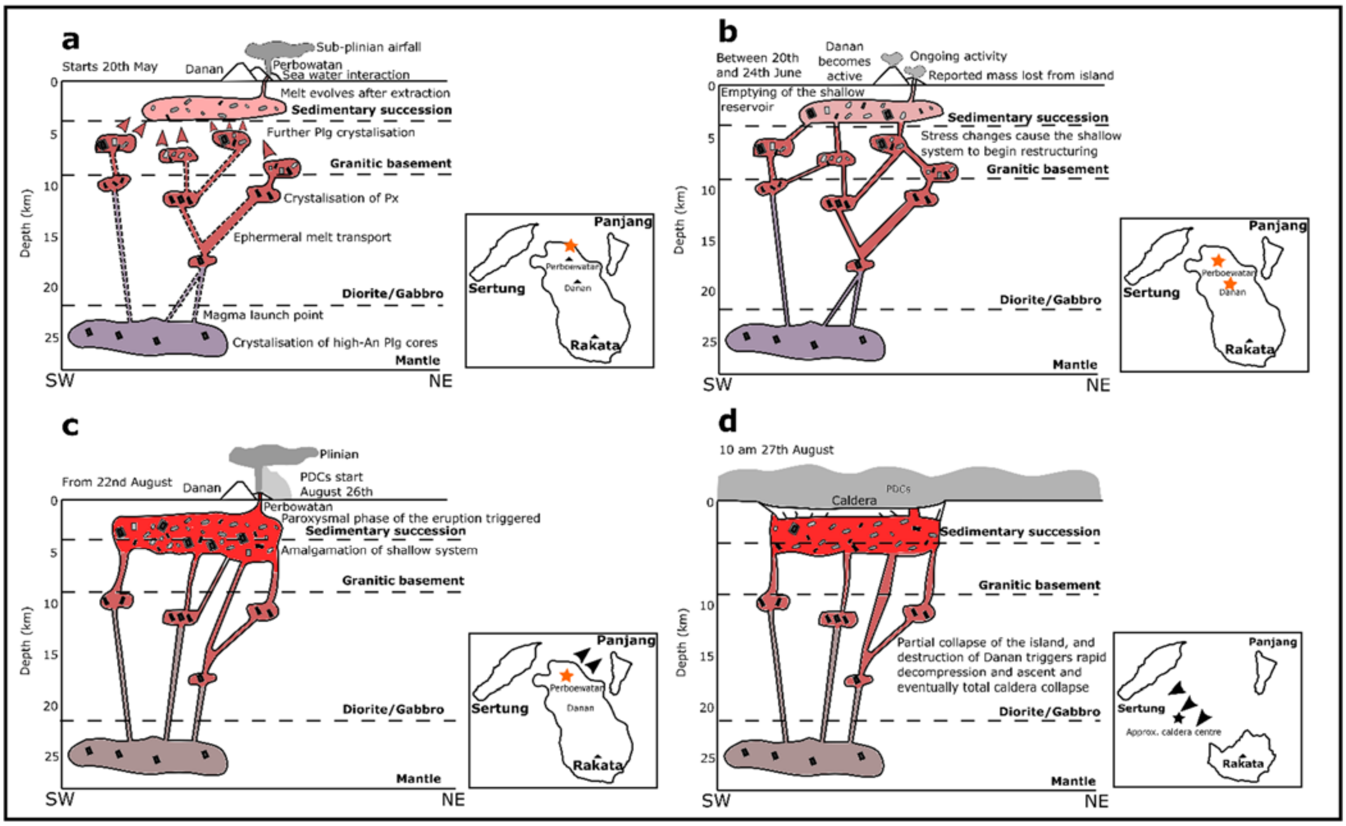

Figure 15: Series of schematic diagrams coupled with plan view maps illustrating the magmatic and eruptive evolution of the 1883 eruption of Krakatau (lithological structure and crystallisation depths from Darhen et al., 2012). On maps orange stars indicate active edifice, and black arrows represent the dominant direction of PDCs. Dashed lines indicate ephemeral transport pathways of magma. Red arrows on schematic diagrams indicate melt extraction. Colours of melt represent melt composition: Purple for the least evolved, followed by brown, bright red, with pink representing the most silicic melt.

6 Conclusions

This study presents field observations from new exposures of the 1883 eruptive deposits of Krakatau, revealed as a result of the removal of vegetation by the 2018 tsunamigenic flank collapse of Anak Krakatau. This has allowed for the stratigraphy of the eruption to be considerably better constrained (Figure 3; Figure 7). Examination of the geochemistry in the context of this refined eruptive stratigraphy (Figure 9) does not support previous studies (e.g. Mandeville et al., 1996a) that have proposed that the eruption emanated from a chemically-zoned magma reservoir. An updated model for the magmatic system is proposed, taking into account the chemical variations in context with the stratigraphic sequence.

Consistent with written accounts (e.g. Symons et al., 1888; Figure 2), the matrix glass chemistry of a distinct, green, basal ashfall (Figures 9 and 14) indicate a shallow, more silicic reservoir was tapped during the precursory activity in May 1883 onwards. It is likely that restructuring of the magmatic system and syn-eruptive mixing of multiple melt batches then occured, to account for the chemical homogeneity in pyroclasts in Units B to D (Figures 9 and 4), and complex plagioclase phenocryst zoning profiles and textures (Figures 10 – 13). This restructuring may have occurred simply as a result of gradual emptying of the initial silicic reservoir, however the loss of mass reported from either or both of the summits of Perboewatan and Danan (Figure 1) may also have played a role. The stress changes and reservoir reconstruction may have contributed to an increase in magma flux observed as an increase in thickness of the eruptive deposits (Figure 7), eventually leading to the onset of the climactic phase of the eruption on 26nd August.

There is a substantial change in the directionality of the PDCs throughout the climactic phase of the eruption (Figure 8), which coincides with the deposition of a lithic lag breccia occupying a distinct horizon within the stratigraphy. The lithic lag breccia is thus attributed to partial collapse of the island, and the removal of the edifice Danan as a topographic barrier. Partial collapse of the island potentially released further overlying pressure on the system, thereby enhancing magmatic ascent, leading to the most explosive and energetic phase of the eruption in the morning of 27th August 1883. This very explosive eruptive phase culminated in total caldera collapse, which, together with the PDC production at this stage, was a potential cause of the largest tsunami at 10 am on 27th August. This final caldera collapse is recorded in the stratigraphy as a second lithic lag breccia, and at one locality (U23/D2S2) lithic lava flow blocks up to 8 m in size are present, which are reported within this sequence for the first time here.

The identification of at least two lag breccias indicates piecemeal caldera formation, where the first stage of collapse is the driving force behind the most energetic and explosive, climactic part of the eruption. Similar magmatic and eruptive behaviour has been documented at other crystal-poor, caldera-forming eruptions occurring in rift zones (e.g., Oruanui; Allan et al., 2012). Precursory Plinian eruptions are therefore very useful phenomena to be aware of for the future monitoring of Anak Krakatau, and perhaps other similar systems, although the identification of such events as precursory to an incipient larger eruption remains challenging. The 1883 eruption of Krakatau, however, provides an example of an event where relatively moderate explosive eruptions may potentially have run-away effects culminating in cataclysmic caldera-collapse several months later.

7 Acknowledgements

With thanks to V. Smith, P. Gopon, J. Wade and E. Johnson for help using electron imaging facilities; O. Green and J. Wells for help with sample preparation; S. Day, S. Carey and S. Self for useful discussions; A. Novellino for help on 2019 field campaign; and the British Geological Survey for the loan of historical samples. DRT and SLE publish with permission of the CEO, British Geological Survey (United Kingdom Research and Innovation).

Funding: This work was supported by the Natural Environment Research Council (NERC). ALM-N acknowledges NERC Studentship NE/L2002612/1; MC acknowledges NERC fellowship NE/N014286/1; MC, SW and SLE acknowledge a NERC urgency grant NE/T002026/1; DMP and TM acknowledge support from NERC COMET.

8 Data availability

Datasets related to this article can be found at https://www.bgs.ac.uk/services/ngdc/accessions/index.html#item137445 , hosted at National Geological Data Centre by the British Geological Survey (Madden-Nadeau, 2020).

9 References

Abdurrachman, M., Widiyantoro, S., Priadi, B. and Ismail, T. (2018). Geochemistry and Structure of Krakatoa Volcano in the Sunda Strait, Indonesia. Geosciences, 8(4), 111.

Algemeen Dagblad (1883). 20th and 26th June, 17th and 27th August, 3rd, 5th and 11th September.

Allan, A.S., Wilson, C.J., Millet, M.A. and Wysoczanski, R.J. (2012). The invisible hand: Tectonic triggering and modulation of a rhyolitic super-eruption. Geology, 40(6), 563-566.

Ashdown, E. (1883). A Floating Lava Bed [Letter to the editor, reprinted from the London Times]. Nature, 28:532-533.

Bachmann, O., Dungan, M.A. and Lipman, P.W. (2000). Voluminous lava-like precursor to a major ash-flow tuff: low-column pyroclastic eruption of the Pagosa Peak Dacite, San Juan volcanic field, Colorado. Journal of Volcanology and Geothermal Research, 98(1-4), 153-171.

Bacon, C.R. (1983). Eruptive history of Mount Mazama and Crater Lake caldera, Cascade Range, USA. Journal of Volcanology and Geothermal Research, 18(1-4), 57-115.

Bacon, C. R. and Hirschmann, M. M. (1988). Mg/Mn partitioning as a test for equilibrium between coexisting Fe-Ti oxides. American Mineralogist, 73(1-2), 57-61.

Bataviaasch Handelsblad (1883). 16th and 28th August, and 9th September.

Bégué, F., Deering, C.D., Gravley, D.M., Kennedy, B.M., Chambefort, I., Gualda, G.A. and Bachmann, O. (2014). Extraction, storage and eruption of multiple isolated magma batches in the paired Mamaku and Ohakuri eruption, Taupo Volcanic Zone, New Zealand. Journal of Petrology, 55(8), 1653-1684.

Bindeman, I. N., Davis, A. M. and Drake, M. J. (1998). Ion microprobe study of plagioclase-basalt partition experiments at natural concentration levels of trace elements. Geochimica et Cosmochimica Acta, 62(7), 1175-1193.

Blake, S., 1984. Volatile oversaturation during the evolution of silicic magma chambers as an eruption trigger. Journal of Geophysical Research: Solid Earth, 89(B10), 8237-8244.

Branney, M. J. and Kokelaar, B. P. (2002). Pyroclastic density currents and the sedimentation of ignimbrites. Geological Society of London.

Brown, S.J.A., Wilson, C.J.N., Cole, J.W. and Wooden, J. (1998). The Whakamaru group ignimbrites, Taupo Volcanic Zone, New Zealand: evidence for reverse tapping of a zoned silicic magmatic system. Journal of Volcanology and Geothermal Research, 84(1-2), 1-37.

Camus, G., Gourgaud, A. and Vincent, P. M. (1987). Petrologic evolution of Krakatau (Indonesia): implications for a future activity. Journal of Volcanology and Geothermal Research, 33(4), 299-316.

Cashman, K. V. and Giordano, G. (2014). Calderas and magma reservoirs. Journal of Volcanology and Geothermal Research, 288, 28-45.

Cassidy, M., Castro, J.M., Helo, C., Troll, V.R., Deegan, F.M., Muir, D., Neave, D.A. and Mueller, S.P. (2016). Volatile dilution during magma injections and implications for volcano explosivity. Geology, 44(12), 1027-1030.

Cassidy, M., Edmonds, M., Watt, S.F.L., Palmer, M.R. and Gernon, T.M. (2015). Origin of basalts by hybridization in andesite-dominated arcs. Journal of Petrology, 56(2), 325-346.

Cassidy, M., Manga, M., Cashman, K. and Bachmann, O. (2018). Controls on explosive-effusive volcanic eruption styles. Nature communications, 9(1), 1-16.

Ceylon Observer (1883). The Volcanic Eruption in the Sunda Straits. 6 Sep.

Charlier, B.L., Peate, D.W., Wilson, C.J., Lowenstern, J.B., Storey, M. and Brown, S.J., (2003). Crystallisation ages in coeval silicic magma bodies: 238U–230Th disequilibrium evidence from the

Rotoiti and Earthquake Flat eruption deposits, Taupo Volcanic Zone, New Zealand. Earth and Planetary Science Letters, 206(3-4), 441-457.

Christopher, T.E., Blundy, J., Cashman, K., Cole, P., Edmonds, M., Smith, P.J., Sparks, R.S.J., and Stinton, A. (2015). Crustal-scale degassing due to magma system destabilization and magma-gas decoupling at Soufrière Hills Volcano, Montserrat." Geochemistry, Geophysics, Geosystems, 16(9), 2797-2811.

Dahren, B., Troll, V. R., Andersson, U. B., Chadwick, J. P., Gardner, M. F., Jaxybulatov, K. and Koulakov, I. (2012). Magma plumbing beneath Anak Krakatau volcano, Indonesia: evidence for multiple magma storage regions. Contributions to Mineralogy and Petrology, 163(4), 631-651.

Deplus, C., Bonvalot, S., Dahrin, D., Diament, M., Harjono, H. and Dubois, J. (1995). Inner structure of the Krakatau volcanic complex (Indonesia) from gravity and bathymetry data. Journal of Volcanology and Geothermal Research, 64(1-2), 23-52.

Druitt, T. H., Costa, F., Deloule, E., Dungan, M. and Scaillet, B. (2012). Decadal to monthly timescales of magma transfer and reservoir growth at a caldera volcano. Nature, 482(7383), 77-80.

Druitt, T. H. and Francaviglia, V. (1992). Caldera formation on Santorini and the physiography of the islands in the late Bronze Age. Bulletin of Volcanology, 54(6), 484-493.

Druitt, T. H. and Sparks, R. S. J. (1982). A proximal ignimbrite breccia facies on Santorini, Greece. Journal of Volcanology and Geothermal Research, 13(1-2), 147-171.

Druitt, T.H., Pyle, D.M. and Mather, T.A. (2019). Santorini volcano and its plumbing system. Elements 15, 177-184.

Edmonds, M. (2008). New geochemical insights into volcanic degassing. Philosophical Transactions of the Royal Society A: Mathematical, Physical and Engineering Sciences, 366(1885), 4559-4579.

Ellis, B.S., Barry, T., Branney, M.J., Wolff, J.A., Bindeman, I., Wilson, R. and Bonnichsen, B., (2010). Petrologic constraints on the development of a large-volume, high temperature, silicic magma system: The Twin Falls eruptive centre, central Snake River Plain. Lithos, 120(3-4), 475-489.

Ellis, B.S. and Wolff, J.A., (2012). Complex storage of rhyolite in the central Snake River Plain. Journal of Volcanology and Geothermal Research, 211, 1-11.

Forni, F., Degruyter, W., Bachmann, O., De Astis, G. and Mollo, S. (2018). Long-term magmatic evolution reveals the beginning of a new caldera cycle at Campi Flegrei. Science advances, 4(11).

Francis, P. and Self, S. (1983). The eruption of Krakatau. Scientific American, 249(5), 172-187.

Furneux (1964). Krakatoa. New Jersey, Prentice Hall.

Gardner, M.F., Troll, V.R., Gamble, J.A., Gertisser, R., Hart, G.L., Ellam, R.M., Harris, C. and Wolff, J.A. (2012). Crustal differentiation processes at Krakatau volcano, Indonesia. Journal of Petrology, 54(1), pp.149-182.

Geschwind, C. H. and Rutherford, M. J. (1992). Cummingtonite and the evolution of the Mount St. Helens (Washington) magma system: an experimental study. Geology, 20(11), 1011-1014.

Ghiorso, M. S. and Evans, B. W. (2008). Thermodynamics of rhombohedral oxide solid solutions and a revision of the Fe-Ti two-oxide geothermometer and oxygen-barometer. American Journal of science, 308(9), 957-1039.

Ginibre, C., Wörner, G. and Kronz, A. (2002). Minor-and trace-element zoning in plagioclase: implications for magma chamber processes at Parinacota volcano, northern Chile. Contributions to Mineralogy and Petrology, 143(3), 300-315.

Gorshkov, G. S. (1959). Gigantic eruption of the volcano Bezymianny. Bulletin Volcanologique, *20*(1), 77-109.

Gottsmann, J. and Marti, J. (eds) Caldera Volcanism: Analysis, Modelling and Response (Dev. Volcanol. 10, Elsevier, 2008)

Grainger (1883). Algemeen Dagblad, 23rd May.

Gravley, D.M., Wilson, C.J.N., Leonard, G.S. and Cole, J.W., (2007). Double trouble: Paired ignimbrite eruptions and collateral subsidence in the Taupo Volcanic Zone, New Zealand. Geological Society of America Bulletin, 119(1-2),18-30.

Grilli, S. T., Tappin, D. R., Carey, S., Watt, S. F., Ward, S. N., Grilli, A. R. and Muin, M. (2019). Modelling of the tsunami from the December 22, 2018 lateral collapse of Anak Krakatau volcano in the Sunda Straits, Indonesia. Scientific reports, 9(1), 1-13

Gualda, G.A., Ghiorso, M.S., Lemons, R.V. and Carley, T.L. (2012). Rhyolite-MELTS: a modified calibration of MELTS optimized for silica-rich, fluid-bearing magmatic systems. Journal of Petrology, 53(5), 875-890.

Hall, R. (2012). Late Jurassic–Cenozoic reconstructions of the Indonesian region and the Indian Ocean. Tectonophysics, 570, 1-41.

Hall, R. and Spakman, W. (2002). Subducted slabs beneath the eastern Indonesia–Tonga region: insights from tomography. Earth and Planetary Science Letters, 201(2), 321-336.

Harjono, H., Diament, M., Nouaili, L. and Dubois, J. (1989). Detection of magma bodies beneath Krakatau volcano (Indonesia) from anomalous shear waves. Journal of volcanology and geothermal research, 39(4), 335-348.

Hesse, E.D. (1690). Ost Indiamische Reise-Beschreibung oder Diariu, Leipzig.

Hesse, E.D. (1694). Drie Seer Aanmerkelyke Reysen na en door Verlerley Gewesten in Oost-Indien; gedaan door Christophorus Frikius, Chirugyn, Elias Hesse, Berghschryver, Christophorus Schweitzer, Boekhouder; Yeder Bysonder; van ‘t Jaer 1675 tot 1686. Translated from German to Dutch by Simon de Vries. Utrecht.

Hildreth, W. and Wilson, C. J. (2007). Compositional zoning of the Bishop Tuff. Journal of Petrology, 48(5), 951-999.

Javasche Courant (1883). 20th July.

Jaxybulatov, K., Koulakov, I., Ibs-von Seht, M., Klinge, K., Reichert, C., Dahren, B. and Troll, V.R. (2011). Evidence for high fluid/melt content beneath Krakatau volcano (Indonesia) from local earthquake tomography. Journal of Volcanology and Geothermal Research, 206(3-4), 96-105.

Joly, J. (1885) Notes on the microscopical character of the volcanic ash from Krakatoa. Proceedings of the Royal Dublin Society, 4, 291-299.

Kamata, H., Suzuki-Kamata, K. and Bacon, C.R. (1993). Deformation of the Wineglass Welded Tuff and the timing of caldera collapse at Crater Lake, Oregon. Journal of volcanology and geothermal research, 56(3), pp.253-265.

Kilgour, G.N., Saunders, K.E., Blundy, J.D., Cashman, K.V., Scott, B.J. and Miller, C.A. (2014). Timescales of magmatic processes at Ruapehu volcano from diffusion chronometry and their comparison to monitoring data. Journal of Volcanology and Geothermal Research, 288, 62-75.

LaTourrette, T. and Wasserburg, G.J. (1998). Mg diffusion in anorthite: implications for the formation of early solar system planetesimals. Earth and Planetary Science Letters, 158(3-4), 91-108.

Latter, J.H. (1981). Tsunamis of Volcanic Origin: Summary of Causes, with Particular Reference to Krakatau, 1883. Bulletin Volcanologique, 44:467-490.

Le Bas, M.J., Le Maitre, R. W., Streckeisen, A., Zanettin, B. and IUGS Subcommission on the Systematics of Igneous Rocks. (1986). A chemical classification of volcanic rocks based on the total alkali-silica diagram. Journal of petrology, 27(3), 745-750.

Lindemann, T.H. (1884). Report from H.B.M Consol at Batavia, inclosing extracts relating to the volcanic outburst in the Sunda Strait, from the logbook of the steamship Governor-General Loudon. Proceedings of the Royal Society of London, 36, 199-203.

Lindsley, D. H. and Frost, B. R. (1992). Equilibria among Fe-Ti oxides, pyroxenes, olivine, and quartz: Part I. Theory. American Mineralogist, 77(9-10), 987-1003.

Lunt, P., Burgon, G., and Baky, A. (2009). The Pemali Formation of Central Java and equivalents: Indicators of sedimentation on an active plate margin. Journal of Asian Earth Sciences, 34(1), 100-113.

MacKenzie (1883). Java Bode, 30 May.

Macleod (1884). De Uitbarsting van de Krakatau. Tijdschift van het Koninklijk Nederlandsch Aardrijk-skundig Genootschap, 2, 1: 184-191 [dataset] Madden-Nadeau, A.L. (2020): Geochemical and petrological data pertaining to the eruptive deposits of 1883 caldera-forming eruption of Krakatau. British Geological Survey. (Dataset). https://doi.org/10.5285/ad2a4fa0-7b66-4ec5-a5cf-d78944716ec4.

Mandeville, C.W., Carey, S. and Sigurdsson, H. (1996a). Magma mixing, fractional crystallization and volatile degassing during the 1883 eruption of Krakatau volcano, Indonesia. Journal of Volcanology and Geothermal Research, 74(3-4), 243-274.

Mandeville, C. W., Carey, S. and Sigurdsson, H. (1996b). Sedimentology of the Krakatau 1883 submarine pyroclastic deposits. Bulletin of Volcanology, 57(7), 512-529.

Mandeville, C.W., Sasaki, A., Saito, G., Faure, K., King, R. and Hauri, E. (1998). Open-system degassing of sulfur from Krakatau 1883 magma. Earth and Planetary Science Letters, 160(3-4), 709-722.

Metzger, E. (1884). Gleanings from Reports Concerning the Eruption of Krakatoa. Nature, 29:240-244.

Mollo, S., Putirka, K., Iezzi, G., Del Gaudio, P. and Scarlato, P. (2011). Plagioclase–melt (dis) equilibrium due to cooling dynamics: implications for thermometry, barometry and hygrometry. Lithos, 125(1-2), 221-235.

Nelson, S.T. and Montana, A. (1992). Sieve-textured plagioclase in volcanic rocks produced by rapid decompression. American Mineralogist, 77(11-12), 1242-1249.

Newhall, C. G. and Dzurisin, D. (1988) Historical Unrest at Large Calderas of the World Vols 1 and 2, Bull. US Geol. Surv. 1855, USGS.

Newman, S. and Lowenstern, J.B. (2002). VolatileCalc: a silicate melt–H_2O–CO_2 solution model written in Visual Basic for excel. Computers and Geosciences, 28, 597-604.

Ninkovich, D. (1976). Late Cenozoic clockwise rotation of Sumatra. Earth and Planetary Science Letters, 29(2), 269-275.

Ninkovich, D. (1979). Distribution, age and chemical composition of tephra layers in deep-sea sediments off western Indonesia. Journal of Volcanology and Geothermal Research, 5(1-2), 67-86.

Nishimura, S., Harjono, H. and Suparka, S. (1992). The Krakatau Islands: the geotectonic setting. GeoJournal, 28(2), 87-98.

Oba, N., Tomita, K., Yamamoto, M., Istidjab, M. and Badruddin, M. (1982). Geochemical study of lava flows, ejecta and pyroclastic flow from the Krakatau Group, Indonesia. Kagoshima Daigaku Rigakubu kiyō. Chigaku seibutsugaku, 15, 41-76.

Rutherford, M. J. and Devine, J. D. (1988). The May 18, 1980, eruption of Mount St. Helens: 3. Stability and chemistry of amphibole in the magma chamber. Journal of Geophysical Research: Solid Earth, *93*(B10), 11949-11959.

Schlüter, H.U., Gaedicke, C., Roeser, H.A., Schreckenberger, B., Meyer, H., Reichert, C., Djajadihardja, Y. and Prexl, A. (2002). Tectonic features of the southern Sumatra-western Java forearc of Indonesia. Tectonics, 21(5), pp.11-1.

Schwandt, C.S., Cygan, R.T. and Westrich, H.R. (1998). Magnesium self-diffusion in orthoenstatite. Contributions to Mineralogy and Petrology, 130(3-4), 390-396.

Self, S. (1992). Krakatau revisited: the course of events and interpretation of the 1883 eruption. GeoJournal, 28(2), 109-121.

Self, S. and Rampino, M. R. (1981). The 1883 eruption of Krakatau. Nature, 294(5843), 699-704.

Self, S. and Wohletz, K. H. (1983). A new look at initiation and timing of the Krakatau 1883 eruption sequence. Eos, 64, 872.

Shields, J. K., Mader, H. M., Caricchi, L., Tuffen, H., Mueller, S., Pistone, M. and Baumgartner, L. (2016). Unravelling textural heterogeneity in obsidian: Shear-induced outgassing in the Rocche Rosse flow. Journal of Volcanology and Geothermal Research, 310, 137-158.

Simkin, T. and Fiske, R.S. (1983) Krakatau 1883: the volcanic eruption and its effects. Smithsonian Institution Press, Washington D.C., 464 pp.

Sparks, R.S.J., Sigurdsson, H. and Wilson, L. (1977). Magma mixing: a mechanism for triggering acid explosive eruptions. Nature, 267(5609), 315-318.

Sparks, R.S.J. and Wilson, C. J. N. (1990). The Minoan deposits: a review of their characteristics and interpretation. Thera and the Aegean world III, *2*, 89-99.

Stehn, C. E. (1929). The geology and volcanism of the Krakatau group. Fourth Pacific Science Congress, 1-54.

Sturdy, E.W. (1884). The volcanic eruption of Krakatau. Atlantic Monthly, 54, 385-391.

Sulzer (1883). Java Bode, 30th May.

Susilohadi, S., Gaedicke, C. and Djajadihardja, Y. (2009). Structures and sedimentary deposition in the Sunda Strait, Indonesia. Tectonophysics, *467*(1-4), 55-71.

Symons, G.J., Judd, J.W., Strachey, S.R., Wharton, W.J.L., Evans, F.J., Russell, F.A.R., Archibald, D. and Whipple, G.M. (1888). The eruption of Krakatoa and subsequent phenomena (p. 494). Trübner & Company.

Tagliche Rundchau (1883). Berlin, 255-256.

Tarasewicz, J., White, R.S., Woods, A.W., Brandsdóttir, B. and Gudmundsson, M.T. (2012). Magma mobilization by downward-propagating decompression of the Eyjafjallajökull volcanic plumbing system. Geophysical Research Letters, 39(19).

Tenison-Woods, J.E. (1884). The Earthquake in the Straits of Sunda. Sydney Morning Herald, 16-18 Jan.

Times of London (1883). 3 July:10, column f, and 8 October.

Tramontano, S., Gualda, G.A. and Ghiorso, M.S. (2017). Internal triggering of volcanic eruptions: Tracking overpressure regimes for giant magma bodies. Earth and Planetary Science Letters, 472, 142-151.

Turner, S. and Foden, J. (2001). U, Th and Ra disequilibria, Sr, Nd and Pb isotope and trace element variations in Sunda arc lavas: predominance of a subducted sediment component. Contributions to Mineralogy and Petrology, 142(1), 43-57.

Van Heerdt, P.T. (1884?) Report of Captain Visman of the Prinses Wilhelmina. Letter to Symons, G.J. at the Royal Society, London.

Verbeek, R.D.M. (1884). The Krakatoa Eruption 1. Nature, 30,10–15.

Verbeek, R.D.M. (1885). Krakatau. Batavia.

Vogel, J.W. (1690). Journal einer Reise aus Holland nach Ost-In-dien. Frankfurt and Leipzig.

Walker (1884). Extracts from log of The Actea (May 20, 1883). Nature, 30.

Waters, L.E. and Lange, R.A. (2015). An updated calibration of the plagioclase-liquid hygrometer-thermometer applicable to basalts through rhyolites. American Mineralogist, 100(10), 2172-2184.

Watt, S.F.L. (2019). The evolution of volcanic systems following sector collapse. Journal of Volcanology and Geothermal Research, 384, 280-303.

Williams, R., Branney, M. J. and Barry, T. L. (2014). Temporal and spatial evolution of a waxing then waning catastrophic density current revealed by chemical mapping. Geology, 42(2), 107-110.

Wilson, C.J.N. and Charlier, B.L.A. (2009). Rapid rates of magma generation at contemporaneous magma systems, Taupo Volcano, New Zealand: insights from U–Th model-age spectra in zircons. Journal of Petrology, 50(5), 875-907.

Wood, B. J. & Blundy, J. D. (1991). Crystal-chemical controls on the partitioning of Sr and Ba between plagioclase feldspar, silicate melts, and hydrothermal solutions. Geochimica et Cosmochimica Acta, 55(1), 193-209.